Energy-saving potential of ground source multiple chillers in simple and hybrid configurations for Mediterranean climates

Alessandro Buscemi, Pietro Catrini [*], Antonio Piacentino, Fabio Cardona, Dhirendran Munith Kumar

Department of Engineering, University of Palermo, Viale delle Scienze, Palermo, Italy

ARTICLE INFO

ABSTRACT

Air conditioning accounts for a large share of energy usage in residential and tertiary sectors. Renewable energy technologies offer promising solutions to reduce the environmental impacts of meeting buildings' energy loads. The possibility of using the soil as a thermal reservoir for heating and cooling systems has gained growing attention in the last decade due to its high potential for energy saving. In this paper, the benefits achievable using ground source chillers for air conditioning in an office building located in Southern Italy are discussed. A multiple chillers system coupled with a borehole heat exchanger is investigated and compared to conventional air-cooled and water-cooled systems. The analysis relies on detailed modeling of the main plant components and exploits a novel approach to calculating the thermal resistance of the borehole. Results show that the ground coupled multiple chillers system achieves a 6.516 average energy efficiency ratio, which is 53.2% higher than the reference air-cooled system and 6.5% higher than the conventional water-cooled system. In addition, a hybrid scheme that integrates the borehole heat exchanger with a cooling tower achieves a 19.5% reduction in make-up water consumption. A sensitivity analysis demonstrates that increasing the borehole depth could lead to a significant variation in the system performance, with different trends for simple and hybrid configurations. The proposed study puts forth a reference for the design and operation of this technology for covering the space-cooling demand of buildings in Mediterranean climates.

1. Introduction

According to the International Energy Agency [1], in 2019 the residential and tertiary sectors accounted for 36.6% of the total final energy consumption in the European Union (EU). Ürge-Vorsatz et al. [2] estimated that heating and cooling in these sectors account for between 18% and 73% of the total energy use. Since fossil fuels were mainly consumed, a large amount of greenhouse gases (GHG) were consequently emitted. The adoption of energy-efficient technologies, the integration of renewable-based sources, and the promotion of efficiency-oriented retrofit interventions represent key actions to increase the sustainability of these sectors. In this regard, Economidou et al. [3] pointed out that the EU has been devoting efforts to reducing energy consumption and the environmental impact of the building sectors by issuing different directives characterized by increasingly stringent energy performance standard to be met by existing buildings and new ones.

Among renewable energy technologies for air conditioning, Geothermal Heat Pumps (GHPs) have been extensively investigated in the literature over the last few decades. GHPs use the ground as a heat source in winter, when the heat pump (HP) is operated in heating mode, and as a thermal sink during summer operation [4]. The relatively stable ground temperature contributes to decreasing the energy consumption of such systems, compared to conventional units whose performances are significantly influenced by the fluctuating temperature of external air [4]. According to Lund and Toth [5], GHPs have the largest geothermal use worldwide, accounting for 71.6% of the installed capacity and 59.2% of the annual energy use. The installed capacity amounts to 77,547 MW_{th} and the energy use is 599,981 TJ/y; these data result from a dramatic increase observed since 2000.

GHPs can be arranged in closed-loop configurations, where heat transfer is achieved by using a ground heat exchanger such as borehole or horizontal heat exchanger pipes (usually indicated as Ground Source Heat Pumps, GSHPs), or in open-loop configurations which use groundwater from a well as a secondary fluid for the heat pumps

---

Nomenclature

A	empirical coefficient of Equations (8)–(9), $[1/(\text{kW})^2]$
B	empirical coefficient of Equations (8)–(9), $[1/\text{kW}]$
C	empirical coefficient of Equation (9), $[\text{kW}]$
$c_{p,w}$	specific heat of the water, $[\text{J}/(\text{kg}\cdot\text{K})]$
C_s	volumetric heat capacity of the soil, $[\text{J}/(\text{m}^3\cdot\text{K})]$
D_b	borehole diameter, $[\text{m}]$
$D_{p,i}$	inner pipe diameter, $[\text{m}]$
$D_{p,o}$	outer pipe diameter, $[\text{m}]$
E_{chiller}	annual electric energy consumption of chillers, $[\text{kWh}_e/\text{y}]$
$\dot{E}_{\text{chiller}}$	electric power absorptions of chillers, $[\text{kW}_e]$
$\overline{EER}$	average energy efficiency ratio [dimensionless]
E_{cooling}	annual energy cooling demand the building, $[\text{kWh}/\text{y}]$
$\dot{E}_{\text{para}}$	electric parasitic power consumptions, $[\text{kW}_e]$
E_{plant}	the total annual electric energy consumption of the plant, $[\text{kWh}_e/\text{y}]$
E_{pump}	annual electric energy absorptions of pumps, $[\text{kWh}_e/\text{y}]$
$\dot{E}_{\text{pump}}$	pump electric power consumptions, $[\text{kW}_e]$
E_{tower}	annual electric energy absorptions of cooling towers, $[\text{kWh}_e/\text{y}]$
$\dot{E}_{\text{tower}}$	cooling tower electric power consumptions, $[\text{kW}_e]$
H_b	borehole depth, $[\text{m}]$
h_{conv}	convective heat transfer coefficient of water within pipes, $[\text{W}/(\text{m}^2\cdot\text{K})]$
$\dot{m}_{w,\text{cond}}$	water mass flow rate of the chiller condensers, $[\text{kg}/\text{s}]$
N_{FC}	number of flux channels of the flow net
N_{TJ}	number of temperature jumps of the flow net
$\dot{q}_b$	heat flux exchanged per unit of borehole length, $[\text{W}/\text{m}]$
$\dot{Q}_{\text{cond}}$	thermal power rejected from the condenser, $[\text{kW}]$
$\dot{Q}_{\text{evap}}$	chillers' cooling capacity, $[\text{kW}]$
$\dot{q}_{\text{geo}}$	local value of the endogenous geothermal flux, $[\text{W}/\text{m}^2]$
R_b	borehole thermal resistance, $[\text{K}\cdot\text{m}/\text{W}]$
R_g	conductive thermal resistance of the grout, $[\text{K}\cdot\text{m}/\text{W}]$
R_p	total thermal resistance across BHE pipes, $[\text{K}\cdot\text{m}/\text{W}]$
T	temperature, $[°\text{C}]$
$\overline{T}_b$	mean borehole surface wall temperature, $[°\text{C}]$
T_{dry}	dry bulb temperature of the air, $[°\text{C}]$

$\overline{T}_{\text{dry}}$	mean annual value of dry bulb temperature of the air, $[°\text{C}]$
$\overline{T}_f$	mean fluid temperature, $[°\text{C}]$
$T_{\text{i\_BHE}}$	temperature of the water entering the BHE, $[°\text{C}]$
$T_{\text{i\_cond}}$	fluid inlet temperature of chiller condensers, $[°\text{C}]$
$T_{\text{i\_tower}}$	water outlet temperature of the cooling towers, $[°\text{C}]$
$T_{\text{o\_BHE}}$	temperature of the water exiting the BHE, $[°\text{C}]$
$T_{\text{o\_cond}}$	water outlet temperature of chiller condensers, $[°\text{C}]$
$T_{\text{o\_tower}}$	water outlet temperature of the cooling towers, $[°\text{C}]$
$\overline{T}_s$	mean value of the undisturbed soil temperature profile, $[°\text{C}]$
T_s	undisturbed soil temperature, $[°\text{C}]$
T_{wet}	wet bulb temperature of the air, $[°\text{C}]$

Greek letters

λ_g	grout thermal conductivity, $[\text{W}/(\text{m}\cdot\text{K})]$
λ_p	thermal conductivity of the pipes, $[\text{W}/(\text{m}\cdot\text{K})]$
λ_s	soil thermal conductivity, $[\text{W}/(\text{m}\cdot\text{K})]$

Acronyms

BHE	Borehole Heat Exchanger
COP	Coefficient of Performance
CT	Cooling Tower
DST	Duct Ground Heat Storage Model
EER	Energy Efficiency Ratio
ESEER	European Energy Efficiency Ratio
EU	European Union
FEM	Finite Element Method
FNM	Finite Net Method
GHG	Greenhouse Gas
GHP	Geothermal Heat Pump
GSHP	Ground Source Heat Pump
GWHP	Ground-Water Heat Pump
HGSHP	Hybrid Ground Source Heat Pump
HP	Heat Pump
PeX	Crosslinked Polyethylene
ESEER	Euopean Seasonal Energy Efficiency Ratio
SEER	Seasonal Energy Efficiency Ratio
TMY	Typical Meteorological Year

(usually indicated as Ground-Water Heat Pumps, GWHPs). Despite their great advantages, the high investment cost required by these technologies still represents a barrier to their widespread use [6]. Many parameters influence the economic viability of these systems, such as local climatic and ground conditions, the availability of alternative efficient heating and cooling systems, and the price of electricity and gas [7].

Several theoretical and experimental papers focused on GHPs have been published over the past decades. Some papers aimed at modeling the behavior of ground heat exchangers [8], and others at performing parametric analyses on the effects of operating conditions on the system performance [9]. Some authors investigated the possibility of driving GSHP using electricity produced by renewable energy [10]. For instance, Kavian et al. [11] investigated the energy and economic performance of a GSHP driven by photovoltaic panels in a residential building in Tehran. It was estimated that a 4% decrease in levelized cost of energy could be achieved with respect to conventional GSHP systems. Litjens et al. [12] investigated the combination of GSHP, photovoltaic panels, and battery storage to lower GHG emissions in urban areas. Based on measured demand data from dwellings in the Netherlands, the authors found that photovoltaic panels could meet around 19% of the GSHP electricity demand, while batteries enhance this by 53%. Other studies investigated the possibility to couple GSHP with thermal energy

storage to lower installation costs and reduce performance degradation over time. For instance, Alavy et al. [13] proposed a phase change material-based thermal caisson for GSHP. The authors estimated that caissons could lead to a 16% improvement in the performance of the systems and a 49% reduction of the capital costs as no additional drilling is required. In another study, Cunha and Bourne-Webb [14] focused on the coupling of HP with a geothermal heat exchanger embedded in buildings' piles. Thermodynamic methods have often been adopted for the analysis of GSHP systems, as well [15]. The possibility of coupling GSHP systems with conventional air-conditioning systems [16] has also been investigated. In such a configuration, the GSHP is used to satisfy the base heating (or cooling) load, the remaining fraction being met by conventional systems such as HPs and boilers (or chillers and rooftop units). When properly sized and operated, these hybrid configurations (briefly indicated as HGSHP) were proven to benefit from both the low investment cost of conventional air-conditioning systems and the low operating costs of GSHPs [17]. When the supplied building has a high cooling demand, an extra cooling device such as a cooling tower (CT) can be effectively integrated into the plant layout to reduce the amount of heat rejected to the ground, thus limiting the increase in ground temperature. Park et al. [18] compared the performance of a GSHP and an HGSHP equipped with a CT operating in parallel and series

configurations with the ground heat exchanger. The coefficients of performance (COP) for the HGSHP with parallel and serial configurations were 18% and 6% higher than that of the GSHP, respectively. In a recently published paper by Bina et al. [19] the benefits achievable using HGSHP, in heating dominant and cooling dominant regions of Japan were investigated. The study revealed that in cooling dominant regions, the BHE length could be halved thanks to the integration of CT, while benefits became negligible in heating dominant regions.

In solar-assisted GHPs, solar thermal technologies such as evacuated tube collectors could contribute to the supply part of heating loads, while decreasing the investment cost and reducing the thermal imbalance. In these configurations, the heat gathered from solar collectors is used to lessen the heat load on ground heat exchangers. Chiasson et al. [20] investigated the use of such a system for a school building in a cold climate, proving that the integration of solar collectors can lead to a 34% decrease in the ground heat exchanger size. You et al. [21] performed an interesting review on design schemes and operation strategies for GSHP integrated with photovoltaic-thermal collectors.

Obviously, in hybrid layouts, the selection of a proper control strategy is of utmost importance to achieve optimal energy performance [8]. In this regard, Gang et al. [22] proposed a control method based on artificial-neural-network predictive models. Hu et al. [23] proposed an extremum-seeking control strategy, while De Ridder et al. [24] used dynamic programming to achieve a global optimal control.

Some papers investigated the potential application of GHPs for air-conditioning in Mediterranean areas, where the viability of such systems is more challenging due to the mild climatic conditions. Marrasso et al. [25] investigated the possibility of coupling a GSHP with a thermal micro-grid to supply a large multi-purpose building in Naples, Italy. The proposed configuration provenly contributed to mitigating the urban heat island phenomenon and achieving high seasonal performance due to the lower temperature fluctuations of the cooling medium compared to external air. Calise et al. [26] investigated the possibility of supplying 5th generation district heating and cooling networks with GWHPs in Spain. Promising primary energy saving and reductions in carbon dioxide emissions were found compared to the reference condition, despite a long payback period. Urchueguía et al. [27] compared the energy performance of a GWHP to an air to water heat pump system for heating and cooling serving an academic building located in Valencia (Spain). For the heating season, the geothermal system allowed for about a 43% reduction in primary energy consumption, compared to the conventional unit. In the cooling season, the average energy saving accounted for nearly 37%. Frau et al. [28] carried out energy and economic analyses for a water-water heat pump serving an air-conditioning system. Results showed that, under the examined conditions, GSHPs are less cost-effective than GWHPs due to their high drilling costs. Blázquez et al. [29] optimized the design of a district GWHP system serving a cluster of buildings and operating in heating and cooling modes. Two design scenarios were analyzed, relying on COMSOL Multiphysics software for optimizing drilling design. Guarino et al. [30] investigated the feasibility of a highly integrated cogeneration system based on solar dish-powered Stirling engines, seasonal geothermal storage, and water-to-water heat pumps for supplying the heat demand of an office building located in Sicily. Naldi and Zanchini [31] assessed the effects of borehole length and HP inverter for a GSHP serving a small residential building, while Lazzarin and Noro [32] analyzed the integration of Photovoltaic/Thermal modules with GSHP for a building in Northern Italy. Iorio et al. [33] developed a numerical model to describe the perturbation induced on the ground by GWHPs serving public schools in Southern Italy. Sakellariou et al. [34] performed energetic and economic analyses of a solar-assisted GSHP serving the heating and hot water demands of a dwelling in Greece. The results showed the design and economic conditions in terms of the number of solar collectors and the financial support mechanism required to achieve economic viability compared to a conventional natural gas-fuelled boiler. Baglivo et al. [35] investigated the possibility to increase the performance of air-cooled HPs in Brindisi

(Italy) by pre-heating/cooling the air supplied to the HP with a horizontal air-ground heat exchanger. Simulation results showed that during the heating season the COP values increase by up to 5.33%, while during the cooling period the energy efficiency ratio (EER) increases by about 10%. Michopoulos et al. [36] compared the energy benefits achievable via GSHPs for meeting air-conditioning demands of residential buildings in Cyprus. It was found that compared to conventional systems, the primary energy savings could range between 1.0 and 7.3 % and between 18.4 and 23.5 % for single-family and multi-family buildings, respectively.

This brief research overview concerning GHP applications for air-conditioning in buildings reveals that most of the studies have focused on GHP operation in heating mode. Besides, some of the few research works which focused on summer operation, assumed that cooling loads were supplied by thermally activated systems. Finally, when the performance of GSHPs in cooling mode had been assessed, simplified models were adopted which would not allow a properly reflection of the operational behavior of the systems (throughout the cooling season), and would eventually affect the reliability of the results [36]. Then, a clear knowledge gap exists regarding the assessment of energy savings achievable by ground-coupled chillers when supplying space cooling in buildings. To quantify the benefits of using the soil as a thermal sink characterized by an approximately constant temperature, rigorous modeling of borehole heat exchangers (BHEs) and heat pumps is required, to reflect the effects of seasonal and daily variations on the operating conditions. To this aim, the present paper considers a multiple chillers system supplying an office building located in Palermo (Sicily). Two alternative layouts are analyzed, one based on conventional ground source multiple chillers and the other on a hybrid configuration that also includes a CT. These two configurations are also compared with conventional air-cooled and water-cooled chillers to quantify the increase in energy performance. Together with the complex set of configurations duly compared, further contributions of the study lie in the two following aspects:

- the increased reliability of results, compared to previous studies based on highly simplified thermal modeling of the system. In particular, the use of accurate performance maps of the reversible HP, along with the detailed modeling of heat exchanges with the ground, allow for a better understanding of plant behavior under variable conditions in terms of cooling load, soil temperature, and dry and wet bulb air temperatures. Indeed, an accurate thermal analysis assessing the ground temperature variations induced by the rejected condensation heat is strictly necessary due to their impact on the return temperature of cooling water and, ultimately, on the efficiency of the chillers.
- a novel approach based on the "flow net method" (FNM) is proposed to derive a simple and explicative expression of the borehole thermal resistance. A transposed use of this graphic sketching method usually applied to solve the Laplace equation governing steady-state seepage through the soil is proposed here, by analogy, to study the conductive thermal flux within the grout mass of the BHE. The application of the FNM also allows for a new physical–mathematical interpretation of the terms of the borehole resistance expression.

The structure of the paper is here outlined as follows. In the second section, detailed modeling of the main plant subsystems is presented. In the third section, the case study is introduced, and the plant configurations are briefly illustrated. In the fourth section, the results are presented and discussed. Finally, conclusions are drawn.

2. Materials and methods

As previously mentioned, accurate modeling of the geothermal system and the reversible HP is crucial to performing a reliable assessment of GSHPs' energy-saving potential. In this section, the models developed

for the main components are briefly presented.

2.1. Geothermal plant model

The considered geothermal system consists of a group of double U-tube vertical BHEs whose features are presented in Fig. 1 and Table 1. To simulate the thermal dynamic response of the system, the Duct Ground Heat Storage Model (DST) developed by Hellström [37] was adopted. This model, already embedded in TRNSYS through Type 557 [38], requires several input parameters, such as the undisturbed soil temperature T_s, the soil thermal conductivity λ_s, and volumetric heat capacity C_s, the number of BHEs and their depth H_b, the mutual distance between the BHEs, the type of connection between the pipes (series or parallel) and the BHE thermal resistance R_b.

The thermal resistance R_b results from the two-dimensional heat transfer across the BHE-soil section under stationary conditions and is defined as shown in Eq. (1),

$$R_b = \frac{\overline{T}_f - \overline{T}_b}{\dot{q}_b} \tag{1}$$

where $\overline{T}_f$ is the mean temperature of the circulating fluid, $\overline{T}_b$ is the mean borehole surface temperature, and $\dot{q}_b$ is the heat flux exchanged per unit of borehole length [39]. For a double U-tube BHE, the thermal resistance R_b can be estimated by Eq. (2) [40],

$$R_b = \frac{R_p}{4} + R_g \tag{2}$$

where R_g is the conductive thermal resistance of the grout, and R_p is the total thermal resistance of the pipes. The latter term is a combination of the conductive thermal resistance across ducts and the convective thermal resistance between the circulating fluid and the internal pipe wall, as described by Eq. (3):

$$R_p = \frac{\ln\left(\frac{D_{p,o}}{D_{p,i}}\right)}{2 \cdot \pi \cdot \lambda_p} + \frac{1}{\pi \cdot D_{p,i} \cdot h_{conv}} \tag{3}$$

where λ_p is the thermal conductivity of the pipes, h_{conv} is the convective heat transfer coefficient within ducts, $D_{p,o}$ and $D_{p,i}$ are the outer and inner pipe diameters respectively. Appropriate correlations for calculating h_{conv} as a function of the mass flow rate in the pipes [41] were included in the model. Besides, well-known equations were implemented for the parametric calculation of distributed and concentrated pressure drops along t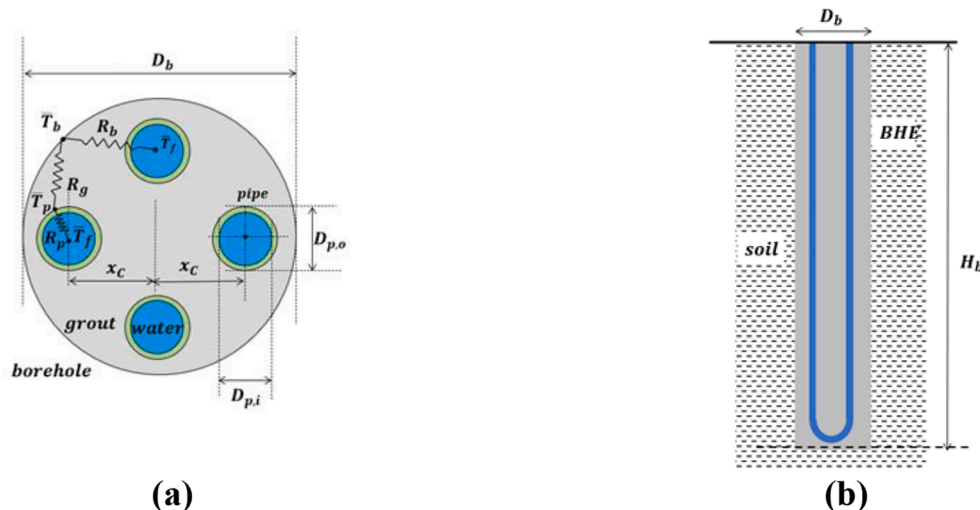he hydraulic circuit [42] also considering different possible connections (either in series or parallel) between the BHE pipes. The pressure drops were then used to calculate the electric power $\dot{E}_{pump}$ consumed by water pumps.

Several approaches have been proposed so far to evaluate the grout resistance R_g of a single U-tube BHE. Some were based on the finite element method (FEM) [43], while others relied on multi-pole methods [40]. These approaches were subsequentially extended to the case of double U-tube BHEs [39,44]. In this paper, the resistance R_g was calculated using the FEM to solve the steady-state heat conservation equation in the space domain described by the data in Table 1. This phenomenon is governed by the well-known Laplace equation [45] expressed in two-dimensional space by Eq. (4):

$$\frac{\partial^2 T}{\partial x^2} + \frac{\partial^2 T}{\partial y^2} = 0 \tag{4}$$

where $T(x,y)$ is the scalar field describing the grout temperature inside the analyzed domain. In this paper, novel use of the FNM to solve the Laplace equation with appropriate boundary conditions is proposed. The FNM is a graph sketching method prevalently used in hydrogeology to analyze the water seepage through the soil [46]. Since the conductive heat flow through the grout material of the BHE follows the same pattern as the groundwater flow through porous media, the transposition of the method is theoretically consistent and allows for an intuitive physical interpretation of the grout resistance.

The flow net corresponding to the graphic solution of the BHE analyzed in this study is depicted in Fig. 2 for a quarter of the total domain. This grid is generated by crossing the heat flow lines (in red) and the isothermal or equipotential lines (in black) so that a square mesh is obtained. According to the FNM theory, if the flow net is made of square meshes, the temperature difference between two consecutive isotherm lines as well as the heat flux of any flow channel bounded by

Table 1
Parameters of the BHEs considered in this study.

Parameter	Value
type of BHE	Double U-tube, Crosslinked Polyethylene (PeX)
pipe outer diameter [m]	0.032
pipe thickness [m]	0.0029
half of the shank space [m]	0.039
PeX thermal conductivity [W/(m·K)]	0.45
BHE diameter [m]	0.140
BHE depth range [m]	120–200

Fig. 1. Transverse (a) and longitudinal (b) sections of a double U-tube BHE with thermal resistances scheme.
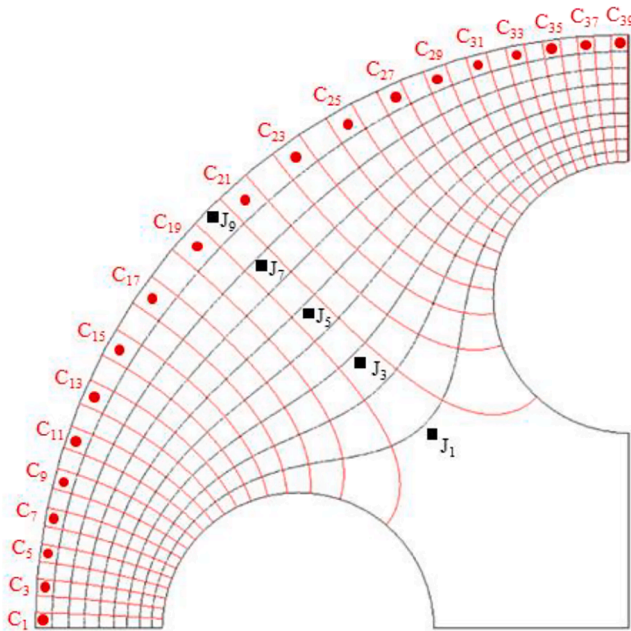
Fig. 2. Flow net for a quarter BHE made up of flow lines (in red) and equipotential lines (in black) generated by FEM.

two adjacent flux lines are constants in the domain.

In the present case, a numerical solution of the Laplace problem was first obtained through a FEM model. Results of this calculation were graphically post-processed to identify the flow net straightforwardly.

Interpreting the FEM solution using FNM theory, it is possible to derive a simple expression of the resistance as shown in Eq. (5):

$$R_{\mathrm{g}} = \frac{N_{\mathrm{TJ}}}{N_{\mathrm{FC}} \cdot \lambda_{\mathrm{g}}} \qquad (5)$$

where λ_{g} is the thermal conductivity of the grout and N_{TJ} and N_{FC} are the number of temperature jumps and flux channels of the flow net, respectively. The above R_{g} expression is formally equivalent to those proposed in the literature, where this quantity is always presented as a ratio between a dimensionless constant and the thermal conductivity of the grout [43]. The expressions usually adopted to calculate this constant are either derived through numerical solutions or deduced through more sophisticated approaches such as the multipole method [40]. These expressions are also a function of the BHE geometry and the ratio of the thermal conductivity of the grout to that of the soil surrounding the BHE. With Eq. (5) a novel physical–mathematical interpretation of the dimensionless constant is proposed, which essentially depends on the flow network solution to the Laplace problem. In the present case, as can be deduced for a quarter BHE shown in Fig. 2, N_{TJ} is 9 (indicated by black squares named by the letter "J") and N_{FC} is equal to 36 (indicated by red circles named by the letter "C"). Then, considering that for the entire BHE, N_{FC} and N_{TJ} are equal to 156 and 9 respectively, from Eq. (5) it follows that R_{g} is equal to 0.058 divided by λ_{g}.

Values of R_{g} calculated with Eq. (5) are about 21% higher than those calculated using the zeroth-order solution obtained by the multipole theory [39] using data from Table 1 and assuming λ_{g} equal to λ_{s}. This result is not surprising since even larger discrepancies can be found between the different solutions proposed in the literature depending on the different BHE geometries and the thermophysical properties of materials [39]. The above R_{g} expression, based on a very accurate FEM solution, was also validated with graph checking based on the FNM. The proposed approach, therefore, can be of considerable help whenever there is uncertainty in estimating the values to be assigned to the thermal resistance of a BHE.

For what concerns the undisturbed soil temperature profile $\overline{T}_{\mathrm{s}}$, a linear increase with depth was assumed, with a gradient related to the local endogenous geothermal flux $\dot{q}_{\mathrm{geo}}$ [47]. The interaction between soil and the atmosphere was modeled assuming a surface soil temperature equal to the average annual dry-bulb air temperature, $\overline{T}_{\mathrm{dry}}$. Thus, a constant value of the undisturbed soil temperature was assumed as input for the numerical model (Type 557 in TRNSYS). This value corresponds to the mean value of the soil temperature in the domain comprised between the soil surface and the BHE depth, calculated by Eq. (6):

$$\overline{T}_{\mathrm{s}} = \overline{T}_{\mathrm{dry}} + \frac{\mathrm{H}_{\mathrm{b}}}{2} \frac{\dot{q}_{\mathrm{geo}}}{\lambda_{\mathrm{s}}} \qquad (6)$$

where $\dot{q}_{\mathrm{geo}}$ can be set equal to the mean geothermal flux in earth continental areas ($\dot{q}_{\mathrm{geo}}$=0.065 W/m^2 [47]).

The above model was implemented in TRNSYS using an equation tool coupled with Type 557. The proposed approach had been previously adopted for a similar case and proven efficient during dynamic multi-year simulations [48]. The numerical model allows the performance of dynamic simulation of heat transfer between a system of BHEs and the circulating fluid, and is suitable for carrying out parametric studies at different mass flow rates and thermal conductivities of the BHE grout.

2.2. Air- and water-cooled chiller models

The main technical features of the air- and water-cooled vapor compression chillers used to develop accurate models and to simulate their behavior are summarized in Table 2. The cooling capacities shown in the table were selected based on the cooling demand peak of the supplied building, which will be presented in Section 3. For all the units, R410A is adopted as the refrigerant, and an electronic expansion valve is used as a metering device. In the water-cooled chiller, brazed plate heat exchangers are used for both the evaporator and condenser. Conversely, in the air-cooled chiller micro-channels and brazed plate heat exchangers are used as condenser and evaporator, respectively.

Each unit is equipped with scroll compressors, induced-draft fans are used at the condenser of air-cooled chillers, while constant speed pumps are installed waterside on the evaporator. The delivered cooling capacity is controlled by activating/deactivating one compressor at a time.

The behavior of chillers at full-load and part-load operating conditions was modeled based on simulations carried out by the tool IMST-ART v.3.80 [49]. Compressor consumption and efficiency were evaluated through the "catalog data" option of the tool, which converts data from a commercial compressors' catalog into built-in consumption and

Table 2
Features of the air-cooled and water-cooled vapor compression chillers.

	Air-Cooled Chiller[a] 520 kW	Water-Cooled Chiller[b] 523 kW
Refrigerant	R410A	
Condenser	Micro-Channels Heat Exchanger	Brazed Plate Heat Exchanger
	10 Fans, 1.2 kW each	2 Pump, 5.5 kW each
Metering Device	Electronic Expansion Valve	
Evaporator	Fin and Tube Heat Exchanger	Brazed Plate Heat Exchanger
	1 Pump, 5.5 kW$_{\mathrm{e}}$	1 Pump, 5.5 kW$_{\mathrm{e}}$
Compressor Type	Scroll	Scroll
Number of compressors	6	6
Compressors Power	172 kW	148 kW
Refrigerant Charge	76 kg	50 kg

The chillers' cooling capacity refers to the following boundary conditions: (a) "Air-Cooled Chiller": variation of the water temperature in the evaporator: 12 °C-7 °C; outdoor air temperature equal to 35 °C. (b) "Water-Cooled Chiller": variation of the water temperature in the evaporator: 12 °C–7 °C; variation of the water temperature in the condenser 30 °C – 35 °C.

efficiency figures that are finally embedded in the simulation algorithm. The tool implements 1-D thermohydraulic modeling of heat exchangers, refrigerant lines, and accessories, and its reliability has been proven by accurate validation against wide sets of experimental results [50]. As regards the metering device, a 3 °C superheat at the evaporator outlet was assumed, in line with the actual operating mode of expansion valves.

Based on simulation results, black-box models of the two chillers were developed and successively implemented in TRNSYS introducing a dedicated macro. For each inlet temperature of the cooling fluid at the condenser, T_{i_cond}, the cooling capacity at the evaporator, $\dot{Q}_{evap}$, and the heat rate rejected to the condenser, $\dot{Q}_{cond}$, under different load conditions were determined. Results obtained for the air-cooled chiller exhibit a relation between $\dot{Q}_{cond}$ and $\dot{Q}_{evap}$ that can be expressed by the quadratic expression presented in Eq. (7),

$$\dot{Q}_{cond} = A \cdot \left(\dot{Q}_{evap} \right)^2 + B \cdot \dot{Q}_{evap} + C \qquad (7)$$

where A, B, and C are three empirical parameters that depend on T_{i_cond}. The values of these parameters were obtained by regression for several operating conditions, and they are summarized in Table 3. Furthermore, an R-square value (R^2) equal to 0.99 was achieved. The model resulting from the combined use of Eq. (7) and the regression coefficients has been proven to be consistent with previous performance maps developed by the authors for air-cooled chillers [30].

In Table 3 an additional column is inserted, referring to the maximum cooling capacity supplied by the chiller at different inlet temperatures of the cooling air. It may be observed that the capacity is extremely sensitive to T_{i_cond}, which also strongly influences the energy efficiency ratio presented in the last column.

A similar procedure was followed for the water-cooled chiller, which led to a simpler quadratic relationship between $\dot{Q}_{cond}$ and $\dot{Q}_{evap}$, as shown in Eq. (8).

$$\dot{Q}_{cond} = A \cdot \left(\dot{Q}_{evap} \right)^2 + B \cdot \dot{Q}_{evap} \qquad (8)$$

The empirical parameters, again obtained by regression of simulation results for the water-cooled chiller, are listed in Table 4. Also, in this case, the R-square value (R^2) was equal to 0.99.

Based on the above model, for each value of T_{i_cond}, the maximum $\dot{Q}_{evap}$ and the regression parameters required to calculate $\dot{Q}_{cond}$ as a function of the current capacity $\dot{Q}_{evap}$ can be easily derived from Tables 3 and 4. Then, in the case of water-cooled chillers, the outlet temperature of water from the condenser T_{o_cond} is simply calculated from the energy balance in Eq. (9):

$$T_{o\_cond} = T_{i\_cond} + \frac{\dot{Q}_{cond}}{c_{p,w} \cdot \dot{m}_{w,cond}} \qquad (9)$$

where $c_{p,w}$ and $\dot{m}_{w,cond}$ respectively indicate the specific heat and the mass flow rate of the cooling fluid through the condenser.

Further, for both types of chillers the electric power absorption can be estimated by Eq. (10):

Table 4
Model parameters at different condenser temperatures for the water-cooled chiller.

T_{i_cond}	$\dot{Q}_{evap,\,max}$	A	B	EER
[°C]	[kW]	[1/(kW)^2]	[1/kW]	[-]
15	614.292	0.000100	1.056	7.85
19	596.781	0.000116	1.065	6.96
23	578.289	0.000137	1.074	6.11
27	558.956	0.000164	1.084	5.36

$$\dot{E}_{chiller} = \left(\dot{Q}_{cond} - \dot{Q}_{evap} \right) + \dot{E}_{para} \qquad (10)$$

where $\dot{E}_{para}$ is the electric parasitic power consumption due to the operation of the water pumps and fans installed in the chillers. More specifically, for the examined case, these consumptions in nominal operating conditions, are set equal to their rated values, i.e., 12 kW$_e$ and 2.70 kW$_e$ for the air-cooled and the water-cooled chillers, respectively.

The black box model described by Eqs. (6)–(9) and Tabs. 3–4 was finally implemented in a TRNSYS macro by coupling it with Type 42 (multi-dimensional data interpolator). The actual performance of the chiller is then accounted for when performing dynamic plant simulations, based on simple input data represented as a function of T_{i_cond} and $\dot{Q}_{evap}$.

2.3. Cooling tower model

To analyze a hybrid configuration where the GSHP system integrates a CT to reject part of the thermal power, a proper model of the tower is required. The operation of a forced draft CT is based on the mass and energy exchange between sprayed water and a stream of air moved by centrifugal fans located in the lower part of the tower. A small portion of the water evaporates, while the remaining chilled water is collected into the tower basin and sent back to the chillers' condenser.

In this study, the VTL-E 149-J open CT of the Baltimore Aircoil Company was selected (main technical features are presented in Table 5), based on the thermal power to be released by the chillers in design conditions. The selected tower, usually installed in small- to medium-scale applications, is characterized by a counter flow configuration.

To predict the performance of this CT, the effectiveness model developed by Braun et al. [51] was used. This model, based on Merkel's theory [52], is already implemented in TRNSYS Type51a and it calculates the water outlet temperature, T_{o_tower}, the water loss rate and the fan power, $\dot{E}_{tower}$, as a function of inlet water temperature and flow rate, dry and wet bulb air temperatures, T_{dry} and T_{wet}, and sump make-up temperature. The model implemented in Type51a was calibrated using 49 performance data at standard conditions provided in compliance with the CTI-201RS standard [53] and publicly available for the VTL-E 149-J unit [54]. For the sake of completeness, the used experimental

Table 3
Model parameters at different condenser temperatures for the air-cooled chiller.

T_{i_cond}	$\dot{Q}_{evap,\,max}$	A	B	C	EER
[°C]	[kW]	[1/(kW)^2]	[1/kW]	[kW]	[-]
17	705.377	0.000264	1.002	6.449	4.63
23	663.104	0.000369	0.976	12.861	3.85
29	620.104	0.000440	0.995	12.527	3.25
35	574.3292	0.000486	1.044	8.885	2.78

Table 5
Technical data of the CT considered in this study.

Parameter	Units	
CT Model	[-]	VTL-E 149-J – Baltimore A. C.
Maximum air volumetric flow rate	[m^3/s]	14
Fan power consumption at maximum flow	[kW$_e$]	5.5
Thermal power rejected	[kW]	588[1]
Water mass flow rate	[kg/s]	28[1]

[1] Condition refers to the variation of the water temperature 35–30 °C, wet-bulb air temperature 26 °C.

data are shown in Fig. 3. More specifically, the rejected heat rate is plotted vs. the wet-bulb temperature of the outdoor air, while considering: (i) different approach temperature, (indicated as ΔT_a), which is equal to the difference between the temperature of the water entering the CT and the air wet-bulb temperature (i.e. $T_{o\_tower} - T_{wet}$); and (ii) different CT range (indicated as ΔT_r), which is equal to the difference between the temperature of the water entering and exiting the CT (i.e., $T_{i\_tower} - T_{o\_tower}$).

3. Description of the case study and the examined plant layouts

A large office building located in Palermo (38.11°N; 13.36°E) was selected as a case study. This site is characterized by mild-wet winters and hot-dry summers, which are typical of the Mediterranean climate. The average air temperature ranges between 21 and 28 °C during the summer season, though it frequently rises above 35 °C and, exceptionally, above 40 °C. The average annual trends of dry and wet bulb air temperatures are depicted in Fig. 4.

The cooling demand profile was derived from an energy audit carried out in a previous study [55]. However, a detailed description of the building is not provided here, since it is not the scope of this paper. The air-conditioning system operates for approximately 960 h in the period between June and September. The annual cooling load of the building, $E_{cooling}$, amounts to 611 MWh$_c$, with a demand peak approximately equal to 1.08 MW$_c$. The cooling demand profile is shown on a second axis in Fig. 4.

In this paper, four alternative plant configurations are analyzed, which are listed below and schematically represented in Fig. 5:

- Configuration "A": multiple air-cooled chillers.
- Configuration "B": multiple water-cooled chillers equipped with cooling towers.
- Configuration "C": multiple water-cooled chillers coupled with BHEs.
- Configuration "D": multiple water-cooled chillers coupled with BHEs and integrating CTs as an additional heat rejection system (also referred to as hybrid configuration).

Configurations A and B are standard options to supply cooling demand in buildings with centralized air-conditioning. They are considered here for the sake of completeness, since they are simply assumed as a reference to assess the improvements in energy performance achieved by the renewable-based configurations C and D.

All four examined multiple chillers configurations include two chillers operated in parallel. Each chiller was sized to cover approximately half of the cooling demand peak, thus resulting in a 520 kW capacity per chiller. Regarding the management strategy, the chillers are supposed to be symmetrically operated, meaning that the cooling demand is equally divided among the chillers [56].

Concerning the BHE in configurations C and D, the number of heat exchangers was set equal to 150 to guarantee that fully turbulent water flow conditions are achieved inside the exchanger pipes. Also, a 150 m BHE depth was assumed.

The average thermophysical properties of the soil in Palermo are summarized in Table 6. Worth noting is that the values of λ_s and C_s reported in Table 6 resulted from a real thermal response test carried out on a pilot borehole in Palermo. Details are not provided here due to the confidential nature of the data. In the same table, the values assumed for the grout thermal conductivity and the corresponding thermal resistance R_g calculated by Eq. (5) are also indicated. Then, based on Eqs. (2)–(3) and considering the R_g in Table 6, the borehole thermal resistance can be calculated; in particular, R_b was found to range between 0.048 and 0.050 (K·m)/W.

3.1. Plant simulations and energy performance indicators

To simulate the dynamic operation of the different plant configurations, the developed models were implemented in TRNSYS [57]. More specifically, the proposed configurations were implemented into four different TRNSYS layouts, including all the main plant components, the auxiliaries, and considering an appropriate control logic for load sharing among the chillers, and pump operation. As an example, in Fig. 6 the TRNSYS layout adopted for configuration D is depicted, where the Types, Macro, and equation tools can be identified. The Typical Meteorological Year (TMY) for Palermo was generated by "Meteonorm" [58], thus providing the hourly-based climatic data as input to calculate the dynamic performance of the air-cooled chillers (configuration A) and the evaporative towers (configuration B and D). The soil and grout parameters presented in Table 6 were also given as input for "Type 557" (BHE model) in configurations C and D. The following main settings were also assumed for this "Type":

- a constant distance between each borehole and its closest neighbor, equal to 12 m.
- an average soil temperature, $\overline{T}_s$, variable with Hb and calculated by Eq. (7) considering the soil thermal conductivity in Table 6 and a
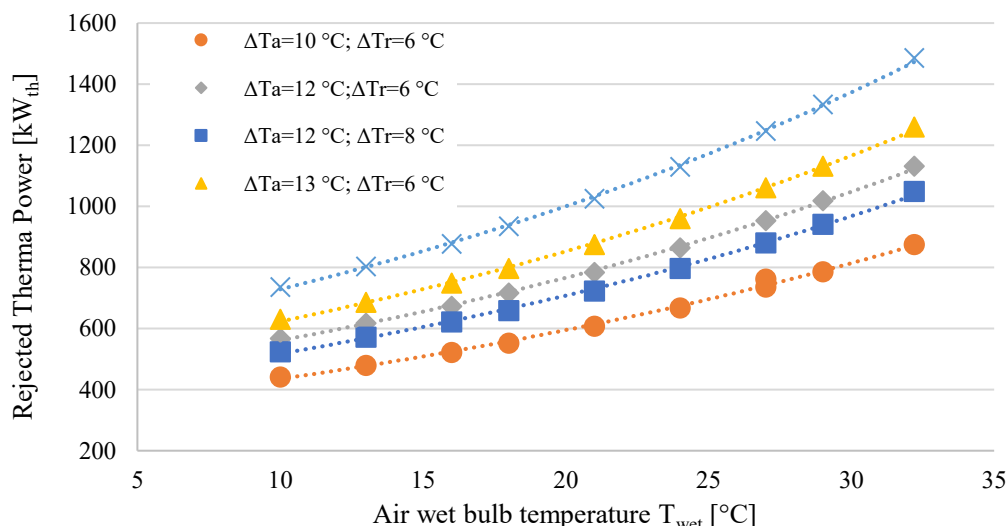

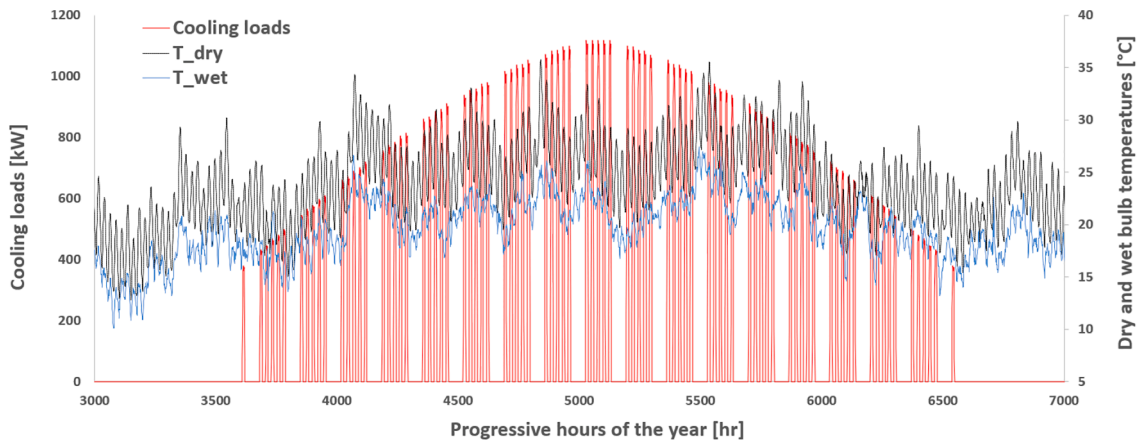**Fig. 3.** CT performance curve elaborated from experimental data available at [54].

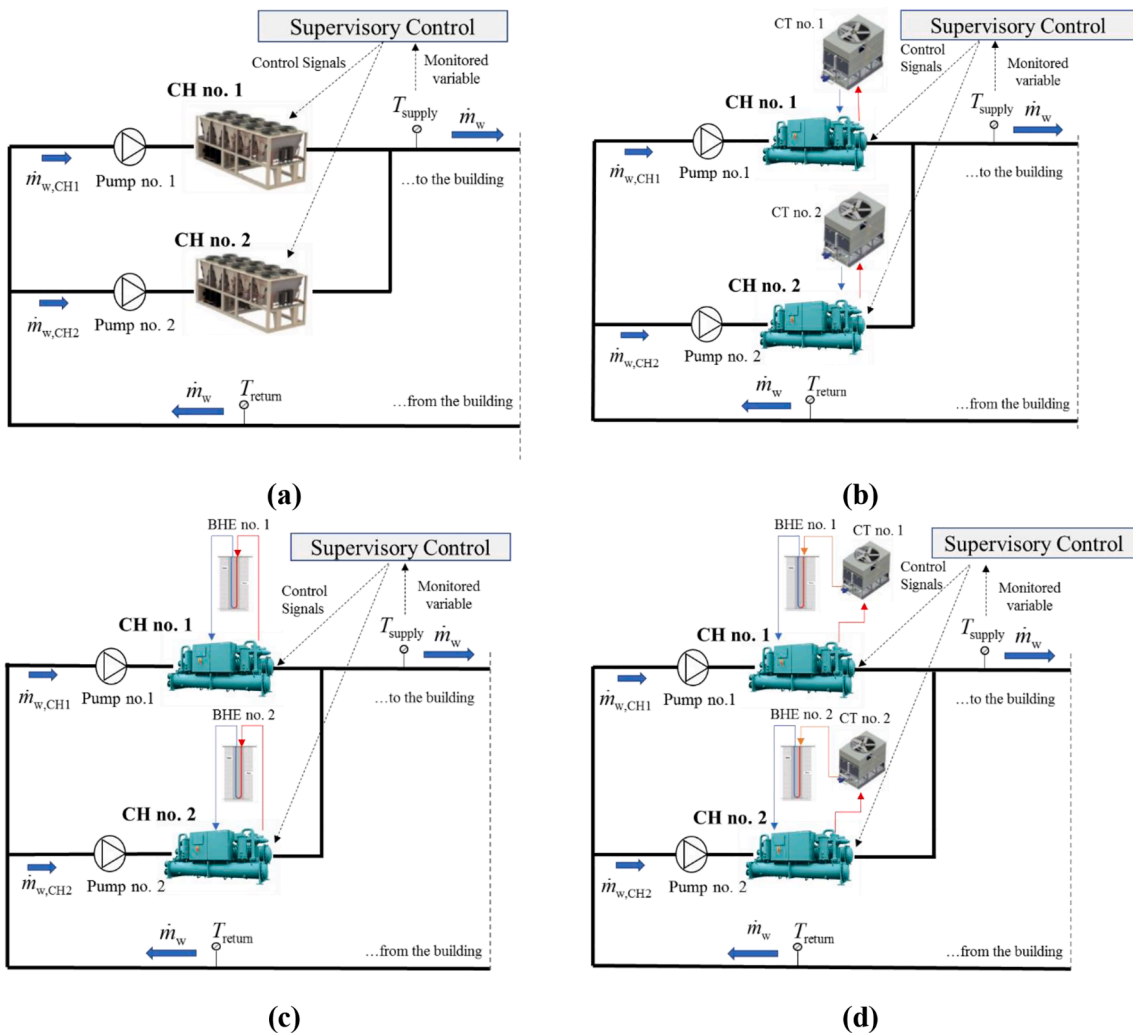**Fig. 4.** Yearly cooling demand profiles and dry and wet bulb air temperatures in Palermo.

Fig. 5. Schematic of the four investigated configurations: (a) multiple air-cooled chiller system; (b) multiple water-cooled chiller system; (c) ground-coupled multiple water-cooled chillers; and (d) hybrid ground-coupled multiple chillers system.

19 °C average dry bulb temperature, $\overline{T}_{dry}$ (this value was derived from the TMY of Palermo).

Note that since these systems are still not adopted in the assumed geographical area, it was not possible to compare the results with experimental data from real existing plants. The only way to validate the results of the simulations was to validate the outputs of each component comprising the analyzed scheme. In this respect, particular attention was paid to the use of models already validated by previous literature studies and to calibrate them using data from real components. For instance, the BHE model used within TRNSYS type 557 was validated against experimental data in recently published papers [59-61] where

Table 6
Soil and grout thermal properties of the site.

Parameter	value
Soil thermal conductivity λ_s [W/(m·K)]	1.75
Soil volumetric heat capacity C_s [MJ/(m^3·K)]	2.72
Grout thermal conductivity λ_g [W/(m·K)]	2.0
Thermal resistance R_g [K·m/W]	0.0288

the difference between measured and predicted output temperature from the BHE always remained below 0.4–0.5 °C. Regarding air- and water-cooled chillers, as previously mentioned, the reliability of results obtained from the tool IMST-ART was already validated in experimental studies such as [50 and 62]. Finally, TRNSYS type51a used for modeling CT operation was validated and calibrated using the real performance data from a commercial system [54].

The energy performance of all the proposed configurations was assessed through hourly-based simulations over the summer season as these systems are designed to supply only building cooling loads. The total annual electricity consumption E_{plant} was calculated for each simulation by integrating over time the following electric power absorption:

- $\dot{E}_{plant} = \dot{E}_{chiller}$ for configuration A.
- $\dot{E}_{plant} = \dot{E}_{chiller} + \dot{E}_{tower}$ for configuration B.
- $\dot{E}_{plant} = \dot{E}_{chiller} + \dot{E}_{pump}$ for configuration C.
- $\dot{E}_{plant} = \dot{E}_{chiller} + \dot{E}_{tower} + \dot{E}_{pump}$ for configuration D.

Based on the above annual electricity consumption, the average energy efficiency ratio ($\overline{EER}$) for each scheme was calculated, based on Eq. (11).

$$\overline{EER} = \frac{E_{cooling}}{E_{plant}} \tag{11}$$

It is worth observing that the previously defined average EER may differ significantly from the Seasonal Energy Efficiency Ratio (SEER) often adopted to compare the performance of different systems on a

seasonal- or whole year- basis. Indeed, while $\overline{EER}$ fits with the definition provided by [63] as "total heat removed from the conditioned space during the annual cooling season divided by the total electrical energy consumed by the air conditioner or heat pump during the same season", it diverges from the standardized procedure used in Europe to calculate the SEER, which is indicated as European SEER (ESEER). Eq. (12) shows the equation used to calculate the ESEER [64],

$$ESEER = \frac{3 \cdot EER_{100\%} + 33 \cdot EER_{75\%} + 41 \cdot EER_{50\%} + 23 \cdot EER_{25\%}}{100} \tag{12}$$

where $EER_{100\%}$, $EER_{75\%}$, $EER_{50\%}$, and $EER_{25\%}$ are the energy efficiency ratios at different part-load conditions assessed at given reference outdoor air temperatures. The approach followed in this study, based on Eq. (11), clearly provides more accurate results than any other based on Eq. (12) [64], since:

- it does not imply the use of reference efficiencies calculated at four operating conditions (each one corresponding to a standard reference condition for the cooling medium) but uses the performance maps to calculate the efficiency on an hourly basis, considering the actual hourly boundary conditions (outdoor air and water return temperatures for air- and water-cooled systems, respectively).
- it does not imply the use of standard "weights" for the cooling energy supplied at different load levels throughout the year, but rather adopting the actual cooling load distribution along the summer period.

Finally, for the configurations that included CTs, the simulations were also aimed at calculating the annual amount of make-up water consumed along the cooling season.

4. Results and discussion

The results of the dynamic simulations carried out for the four examined configurations are presented and discussed in the following subsections. Some insights on the plant operation are also given to allow for a keener interpretation of the interactions among plant components.
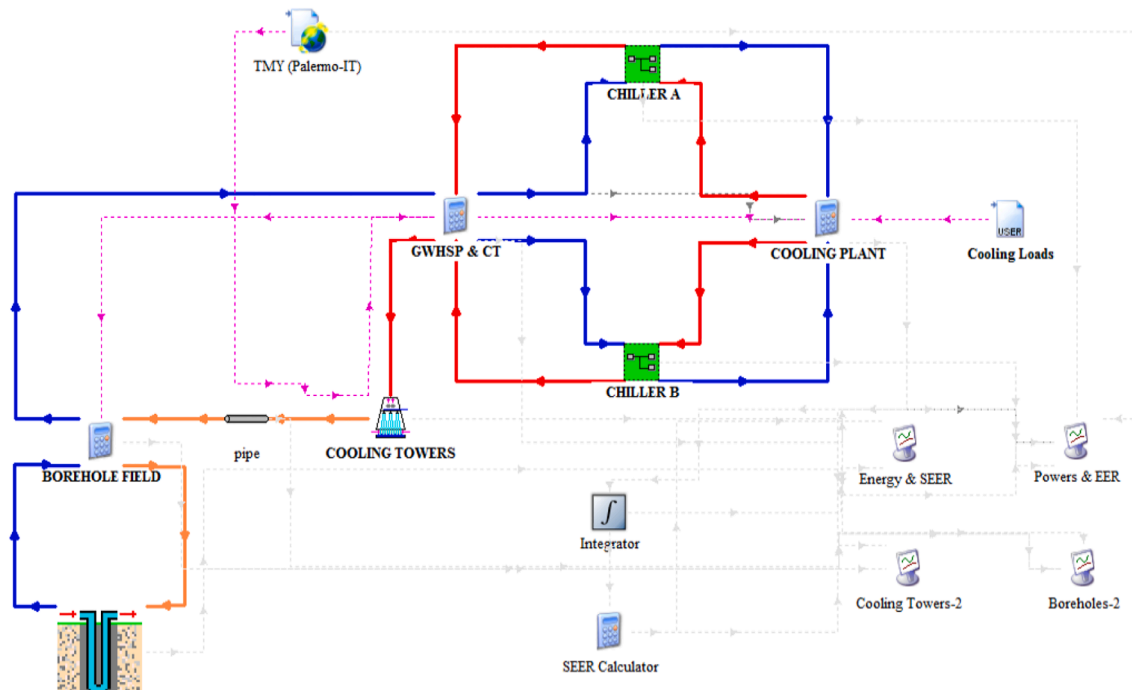
Fig. 6. TRNSYS layout of the hybrid configuration D composed of two chillers, two CTs, and a set of 150 BHEs.

4.1. Results obtained for the reference air- and water-cooled multiple chillers systems

Through simulations performed for configuration A, it was found that 142.58 MWh$_e$/y electricity (E_{plant}) was consumed on an annual basis to supply the building load, $E_{cooling}$, equal to 611.4 MWh$_c$/y. Then, based on Eq. (12), an $\overline{EER}$ equal to 4.283 resulted.

Regarding configuration B, which includes two water-cooled chillers equipped with CTs, an $\overline{EER}$ equal to 6.113 was found. In this case, indeed, supplying the same cooling load implied a 100.08 MWh$_e$/y annual electricity consumption, resulting as the sum of the annual consumption to drive the chillers, $E_{chiller}$ = 90.71 MWh$_e$/y, and the additional consumption by the CTs, E_{tower} = 9.37 MWh$_e$/y. Besides, in this configuration, the annual volume of make-up water consumed by the CTs amounted to about 971 m^3/y.

In Fig. 7.a-b, for this configuration the hourly profiles of inlet and outlet cooling water temperature to and from the condenser, EER, and wet-bulb temperature of the outdoor air are shown for two working days, more specifically July 29th (Fig. 7.a) and September 24th (Fig. 7.b). These two days were selected as "high" and "low" cooling load scenarios, since they exhibit different demand peaks equal to 1,118 kW$_c$ and 480.6 kW$_c$, respectively. Also, very different wet-bulb temperatures of outdoor air (bold black lines in the figure) are observed.

From a comparison between the gray-dashed lines, it is apparent that much lower EER is achieved during the hot day (characterized by high cooling demand). Looking more in-depth at the results, it may be observed that:

- this trend is primarily related to the prevalent operation of the chillers at full or high load during the hot day, as evident from the lowest EER values achieved during peak hours from 12.00 a.m. to 6.00p.m. (corresponding to the hours 5,028–5,034 in Fig. 7.a).
- the average temperature of the cooling medium plays a non-negligible effect in worsening the chillers' performance during high load periods. Indeed, much higher water inlet temperatures at the condenser, T_{i_cond}, are observed in Fig. 7.a, as an obvious consequence of the CT performance that is strongly affected (see Fig. 3) by the external air wet-bulb temperature, T_{wet}. Since the average T_{wet} is equal to 24.51 °C on July 29th and 20.63 °C on September 24th, the water inlet temperature at the condenser was found to be approximately 5 °C higher during the hot and humid day. An even higher difference may be observed for the outlet temperature of cooling water (red lines in Fig. 7.a-b) since its temperature increase across the condenser (measured by the gap between the red and light blue lines) is proportional to the heat rejection rate.

These results prove that despite their better performance compared to air-cooled chillers, even in water-cooled systems there is a relevant scope for seeking improved solutions to guarantee efficient heat rejection when prolonged high load periods are observed during the summer season. The EER and temperature profiles in Fig. 7.a-b provide a reference for a comparison with the results achieved by the two geothermal configurations that are discussed in the following subsections.

4.2. Results obtained for the multiple chillers systems coupled to a borehole heat exchanger

Regarding configuration C, results of hourly simulations carried out for a BHE with depth H_b = 150 m are shown in Fig. 8, where profiles of the water inlet and outlet temperatures to and from the condenser, T_{i_cond} and T_{o_cond}, and the average soil temperature $\overline{T}_s$ are depicted over the whole summer period. It may be observed that the water temperature at the condenser outlet, which also represents the temperature at which it returns to the BHE system, is highly influenced by the cooling load, increasing with the load and the consequent amount of heat to be rejected at the condenser. The load also influences the temperature of the water exiting the BHE (indicated as inlet temperature to the condenser, T_{i_cond}). However, it exhibits slightly lower fluctuations compared to those observed in configuration B, since it is also dependent on the local soil temperature. In this regard, a large distance between the BHEs being assumed (in the order of 12 m), the annual thermal energy rejected to the soil amounting to 678.96 MWh$_{th}$ resulted in the induction of a very limited thermal drift, 0.2 °C, the average soil temperature $\overline{T}_s$ negligibly increasing from an initial value of 22.71 °C to 22.91 °C at the end of the summer season. Different results would have been achieved if a lower distance between the BHEs was assumed, resulting in a higher soil temperature drift as will be discussed in a sensitivity analysis below in the paper.

The seasonal results of plant operation are shown in Table 7. The annual electricity consumption of the chillers was equal to 93.78 MWh$_e$/y, with an additional consumption for pumping that accounts for less than 6% of the total consumption. An $\overline{EER}$ equal to 6.172 was found. In addition, for configuration C no water is consumed due to the absence of CTs.

The scale of representation adopted in Fig. 8 to detect seasonal trends of the main operating temperatures does not allow for a deeper interpretation of daily temperature profiles. To better illustrate the BHE performance and its influence on the water temperature and the EER, in Fig. 9.a-b the simulation results are presented for the same working days considered in section 4.1 in Fig. 7.a,b. More specifically, the daily profiles of T_{o_cond}, T_{i_cond}, and $\overline{T}_s$ obtained for July 29th and September 24th
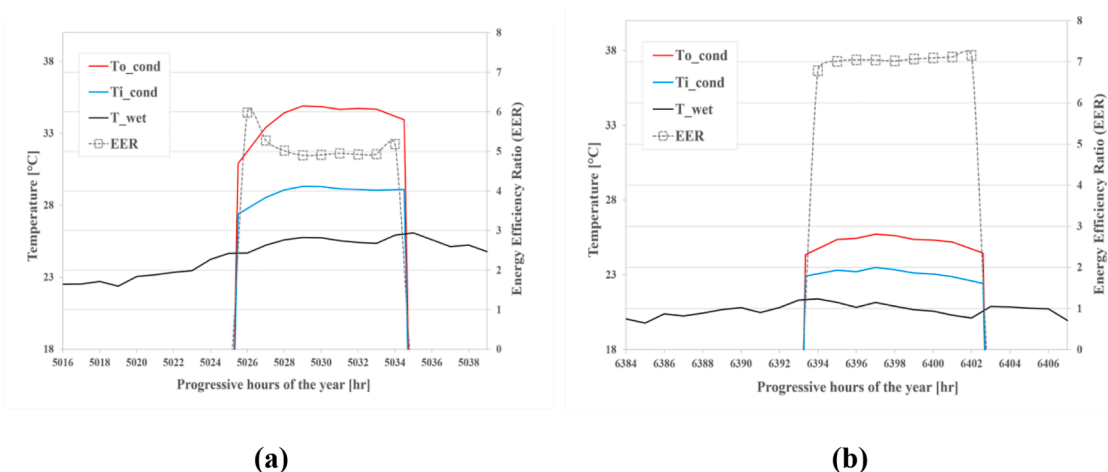

Fig. 7. Configuration B: Temperature and EER hourly profiles on a **(a)** typical hot day (July 29th) and **(b)** typical warm day (September 24th).
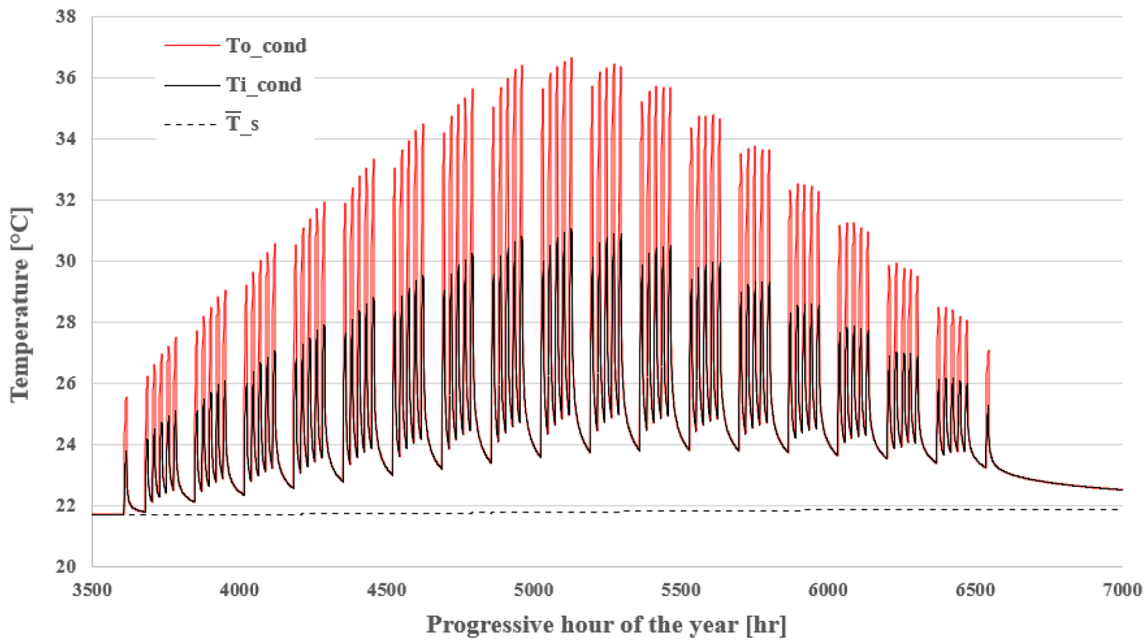
Fig. 8. Configuration C (H_b = 150 m): variations in T_{o_cond}, T_{i_cond}, and $\overline{T}_s$ from June to September.

Table 7
Configuration C: annual values of energy and water consumption.

	Units	Value
$E_{chiller}$	[MWh$_e$/y]	93.78
E_{pump}	[MWh$_e$/y]	5.38
$\overline{EER}$	[-]	6.172
Water Consumption	[m^3/y]	–

are respectively shown in Fig. 9.a-b. Also, the values of $\overline{T}_b$ (i.e., the average temperature at the interface between the concrete grout of the BHE and the surrounding soil) are plotted. It may be observed that:

- during the day with high cooling demand (see Fig. 9.a), the water inlet temperature at the condenser (light-blue continuous lines), T_{i_cond}, increases from 23.8 to approximately 30 °C. By comparing this profile with the one presented in Fig. 7.a, it can be noted that the replacement of CTs with BHEs leads to a moderate decrease in the average water temperature mainly during the first few hours of daily operation. Consequently, there is slight increase in the *EER* values achieved by configuration C. Conversely, negligible effects are

observed between 2.00 and 6.00p.m. (hours indicated as 5,030–5,034 in the figure).

- during the day characterized by low cooling demand (Fig. 9.b), the water inlet temperature at the condenser observes a slight increase from 23.8 to 26.4 °C. By comparing this profile with the one shown in Fig. 7.b, it can be observed that the average daily temperature of the water supplied to the condenser in configuration B, equal to 23.1 °C, is lower than the corresponding value in configuration C, i.e., 24.6 °C. Such a difference is explained by considering that in configuration B the presence of CT makes T_{i_cond} dependent on the air wet-bulb temperature, T_{wet}, which assumes an average 20.6 °C value during this moderately warm day. Conversely, in Configuration C the bottleneck for lowering the cooling water is represented by the temperature of the soil, $\overline{T}_s$, which remains approximately constant at 22.7–22.9 °C throughout the whole summer season. The different values of these two limiting temperatures are then responsible for the slightly higher temperature of the cooling medium (and the consequently higher condensation pressure) achieved by configuration C during this "low cooling load" day. Despite this minor drawback, this geothermal configuration achieves a slightly higher EER than configuration B (as evident from a comparison between the gray
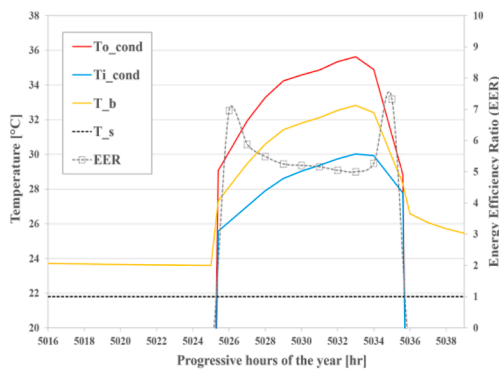
(a)
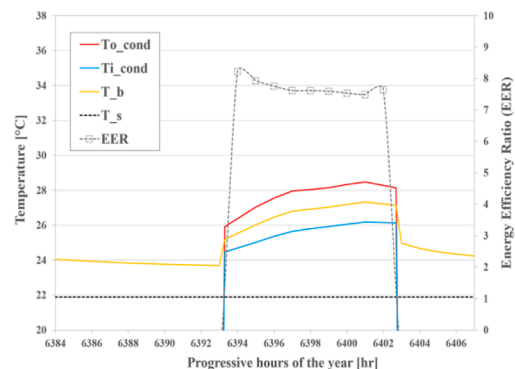
(b)

Fig. 9. Configuration C: Temperature and EER hourly profiles on a **(a)** typical hot day (July 29th) and **(b)** typical warm day (September 24th).

dashed lines in Fig. 7.b and 9.b) due to the lower energy consumption for water pumping in the BHE compared to the electricity consumption for CT' fan operation.

4.3. Results obtained for the multiple chillers systems coupled to a borehole exchanger integrated with cooling towers

In analogy with the approach followed for the previous configuration, before discussing the annual energy results achieved by configuration D, it is worth analyzing the seasonal and daily temperature profiles obtained for the water-cooled chillers served by the integrated "BHE + CTs" system.

In Fig. 10, the temperature of the water entering and exiting the BHE, T_{i_BHE}, and T_{o_BHE}, along with the average temperature of the soil $\overline{T}_s$ are presented yearly. These temperatures are no longer indicated as T_{o_cond} and T_{i_cond} (notation used in Fig. 8) as the water outlet temperature from the condenser does not coincide with the inlet temperature to the BHE and consequently to the series arrangement between the BHE and the CTs (conversely, T_{o_BHE} still coincides with T_{i_cond}, see Fig. 5.d). The water temperature profiles shown exhibit much higher fluctuations than those observed for configuration C in Fig. 8, since T_{i_BHE} essentially depends on the efficiency of water precooling at the CT, which is in turn influenced by the highly variable air wet-bulb temperature, T_{wet}. The thermal drift of the soil mass, 0.05 °C, is even lower than the one observed in Fig. 8 so it cannot be detected at the representation scale in the figure. This reduction in the thermal drift descends from the fact that in configuration D the thermal power of the cooling water is partly dissipated by the CTs, with a residual amount of thermal energy dissipated to the soil mass equal to 175.34 MWh/y.

The annual electricity consumption, the water consumption, and the seasonal average $\overline{EER}$ resulting from the yearly simulation of configuration D are summarized in Table 8.

In Fig. 11.a-b the daily profiles of T_{o_cond}, T_{o_tower} (coincident with T_{i_BHE}), T_{i_cond}, T_{wet}, and $\overline{T}_s$ are depicted for the same working days considered so far. Additional information is provided in Fig. 11.c-d where the thermal power rejected on an hourly basis during the same two days is shown, with a further distinction between the fractions dissipated by the CTs (blue bars) and BHEs (orange bars). It may be observed that:

Table 8
Configuration D: annual values of electric absorption, EER, and water consumption.

	Value
$E_{chiller}$ [MWh$_e$/y]	79.936
E_{tower} [MWh$_e$/y]	9.372
E_{pump} [MWh$_e$/y]	4.585
$\overline{EER}$ [-]	6.516
Make-up water [m³/y]	781.6

- on the day characterized by higher cooling loads (see Fig. 11.a), the water temperature at the condenser inlet, T_{i_cond} (light-blue continuous lines) varies between 22.3 °C and 25.4 °C. By comparing this profile with the one shown in Fig. 9.a for configuration C, it is evident that the inclusion of CTs in series with BHEs to pre-cool the fluid leads to a substantial decrease in the average temperature T_{i_cond} of the water supplied to the condenser for all operating hours. The reduced temperature of the cooling water leads to a reduction in the condensing pressure of the chillers, and then to an improvement in performance as testified by the much higher EER values achieved throughout the day, with an average 6.20 value (compared to the 5.2 average daily EER achieved by configuration C). Looking at Fig. 11.c, it may be observed that under such heavy cooling load conditions, the CT allows the discharge of approximately 50% of the condensation heat, the remaining fraction being dissipated by the BHE to the soil mass.

- on the day with low cooling demand (see Fig. 11.b), the water temperature at the condenser's inlet experiences only moderate variations between 22.1 and 22.6 °C. A simple comparison with the trends shown in Fig. 9.b for configuration C allows the observation that even on such a moderately warm day the inclusion of the CTs leads to a substantial decrease in the average temperature of the water supplied to the condenser. In this case, the benefit is mainly related to the excellent performance of the CTs for water pre-cooling, related to the favorable external air conditions. In fact, as evident in the figure, the air wet-bulb temperature, T_{wet} (black-bold line in Fig. 11.b) is lower than the temperature of the soil $\overline{T}_s$ (almost horizontal, black-dashed line) throughout the whole day. The series connection between the two components and the favorable conditions for the operation of CTs mean the tower plays a prevalent role in the discharge of condensation heat, as evident in Fig. 11.d. A
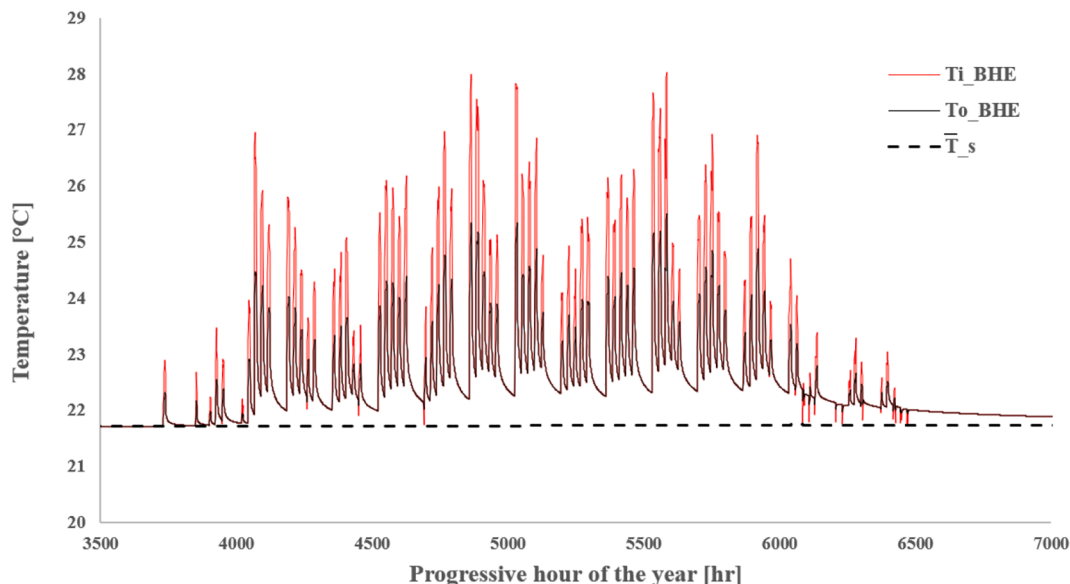
Fig. 10. Configuration D (H_b = 150 m): variations of T_{i_BHE} and T_{o_BHE} and $\overline{T}_s$ from June to September.
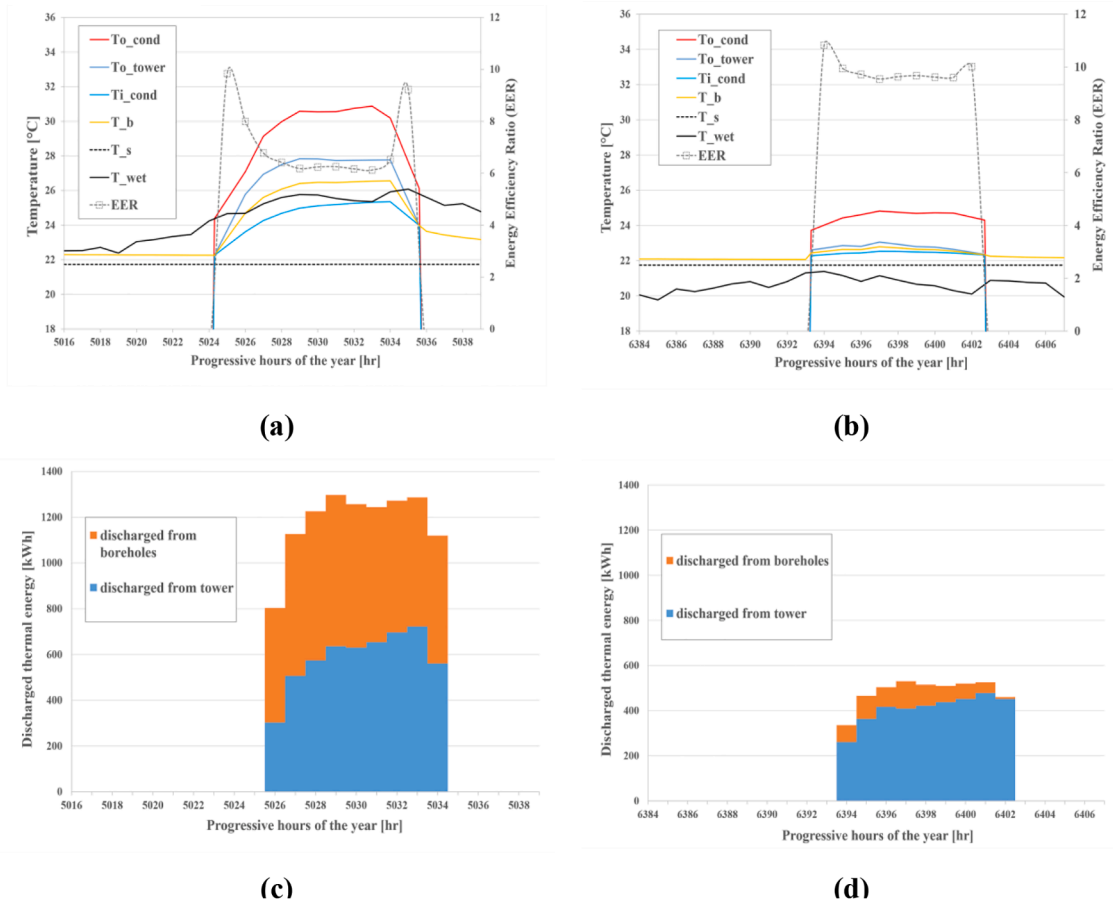
Fig. 11. Configuration D: **(a)** Temperature and *EER* hourly profiles on a typical hot day (July 29th); **(b)** temperature and EER hourly profiles in a typical hot day (July 29th) and typical warm day (September 24th); **(c)** thermal power discharged by the BHE and CTs on July 29th; and **(d)** thermal power discharged by the BHE and CTs on September 24th.

simple comparison between the blue and the orange bars indicates that almost 80% of the heat content of cooling water is dissipated to air via the CTs. The limited amount of heat released by the BHE makes its temperature T_b assume much lower and stable values than those assessed for configuration C and shown in Fig. 9.b. Finally, the reduced temperature of the cooling water flowing through the condenser induces a reduction in the condensation pressure and a consequent increase in the *EER*. The average daily *EER* value achieved by configuration D, equal to 9.7, represents a serious improvement compared to the average *EER* achieved by configuration C, approximately equal to 7.7 (see dashed-gray lines in Fig. 11.b and 9.b, respectively).

4.4. Comparison of the four alternative plant configurations

A brief comparative analysis of the results found for the proposed configurations is due. In Table 9, the annual electricity consumption E_{plant}, $\overline{EER}$, and water consumption values are shown. Worth noting that the comparison was performed considering that the same $E_{cooling}$ value was almost delivered by each configuration on an annual basis (around 611 MWh$_c$/y). As shown, the minimum value for the electricity consumption was found for configuration D. This value is approximately 5.3 MWh$_e$/y lower than the energy consumption of configuration C (−5.34%), 6.2. MWh$_e$/y lower than configuration B (−6.2%), and 48.7 MWh$_e$/y lower than configuration A (−34.1%). The latter values point out that energy saving could be achieved via multiple chillers systems coupled with a BHE (hybrid or not), especially compared to air-cooled chillers (usually adopted for cooling provision in the tertiary sector).

Table 9
Annual values of electricity consumption, SEER, and water consumption for the investigated configurations.

	Configuration			
	A	B	C	D
E_{plant} [MWh$_e$/y]	142.579	100.081	99.156	93.893
$\overline{EER}$ [-]	4.288	6.113	6.172	6.516
Water Consumption [m^3/y]	–	971	–	781.6

Looking at $\overline{EER}$, the same values were found comparing configurations C and B because of similar E_{plant} values. However, almost 971 m^3/y of water consumption is avoided passing from configuration B to C due to the absence of a CT.

A slight increase in $\overline{EER}$ was observed comparing configurations D and B due to lower E_{plant} values. Besides, about 189.4 m^3/y less water is consumed (−19.5%) by the CT in configuration D.

Finally, when comparing configurations C and D, two opposing benefits are observed. Indeed, although a slight increase in the $\overline{EER}$ value was observed passing from C to D due to the reduction in E_{plant} (i.e. −5.3 MWh$_e$/y), almost 781.6 m^3/y water must be consumed in the hybrid configuration.

4.5. Sensitivity analyses

Some sensitivity analyses were performed for the proposed application, aimed at pointing out the influence of some key design param-

eters on plant performance and the annual energy saving. More specifically, the sensitivity of $\overline{EER}$ and water consumption with the BHE depths and the distance among BHEs within the geothermal field were assessed for both configurations C and D.

4.5.1. Sensitivity of system performance to BHE depth

Simulations were carried out for the simple and hybrid geothermal configurations C and D, assuming a fixed distance between the BHEs equal to 12 m and varying the BHE depth ranging from 20 to 250 m. In Fig. 12, the results are shown in terms of seasonal average energy efficiency ratio, $\overline{EER}$, and, regarding configuration D, also presenting the annual consumption of make-up water.

For both configurations, the $\overline{EER}$ curve shows first an increasing and then a decreasing trend as the BHE depth is increased. A physical interpretation of these trends lies in the fact that by increasing the depth of the probes, the average temperature of the soil $\overline{T}_s$ also increases due to the endogenous geothermal gradient. Therefore, there is a limiting depth above which the EER begins to decrease since the benefits arising from the additional heat exchange surface are overcome by the effects of the higher local soil temperature. This depth guaranteeing a maximum $\overline{EER}$ is equal to about 230 m for configuration C, and 130 m configuration D. These values should not be intended as "optimal depths", being based exclusively on an energy performance assessment; the optimal depth of BHEs is influenced prevalently on the installation costs, the analysis of which is beyond the scope of this paper.

For configuration C, for instance, only a 12.28% increase in the $\overline{EER}$ value is achieved when the BHE depth passes from 80 to 230 m. Similarly, for configuration D an increase in BHE depth from 20 to 130 m only induces a slight $\overline{EER}$ increase from 6.28 up to 6.52.

Regarding the annual water consumption from the CTs in configuration D, a minimum value is obtained for a BHE depth of 120 m, which also lies on the flat interval of the $\overline{EER}$. Then the whole BHE depth interval (110 m; 130 m) would result in quasi-optimal plant designs from both an energy- and a water-saving perspective. In general terms, configuration D seems preferable to configuration C, since it allows a higher $\overline{EER}$ to be achieved with a much lower BHE depth and tubes' length.

4.5.2. Sensitivity of system performance with BHE distance

Simulations were carried out for configurations C and D, assuming a field BHE depth of 150 m and varying the distance between the

geothermal borehole in the range of 3–18 m. The results are shown in Fig. 13, in terms of $\overline{EER}$ and annual soil thermal drift, presented on the two vertical axes. The values of soil thermal drift were obtained as the difference between the average soil temperature at the end of the first year of operation and the undisturbed initial soil temperature.

In both the examined configurations, it was found that $\overline{EER}$ improves when the distance between the probes is increased. However, such an increase is significant for the simple geothermal configuration, and much slighter for the hybrid one. Above a threshold distance in the order of 7–8 m, the $\overline{EER}$ assumes an almost constant value for each configuration. These results perfectly comply with a well-known rule of thumb in the sector, which recommends maintaining the distance between geothermal probes above a minimum limit in the 7–9 m range to minimize the effect of mutual thermal interference. On the other hand, the soil thermal drift monotonically decreases when increasing the distance between the probes. For configuration C, for example, at distances lower than 6 m between the boreholes the annual increase in the average soil temperature is above 1 °C. Such a condition would not be acceptable, since after 10 years of operation a soil temperature increase in the order of 10 °C would result, with a consequent dramatic reduction of the plant performance in terms of EER. Conversely, when distances between neighbor probes higher than 10 m are concerned (see Sections 4.2 and 4.3, where a 12 m distance was assumed), the annual thermal drift is much lower, and effective plant operation can be achieved for many years.

5. Conclusions

In this paper, the energy performance of multiple chillers systems coupled with a BHE was investigated. In particular, the assumed system was designed to meet the cooling requirements of an office located in the Mediterranean area. Two different layouts, based on conventional ground source multiple chillers and on a hybrid configuration also including a CT, were simulated and compared with two reference and non-geothermal configurations. Besides, thanks to FNM theory, a new physical–mathematical interpretation of the BHE thermal resistance was proposed. To assess the energy performance over a whole year, detailed models developed for all the main plant components were solved by hourly-based simulations.

Results revealed that compared to multiple air-cooled chillers, simple and hybrid ground source multiple chillers configurations could lead to a 34% reduction in energy consumption. As expected, the increase in
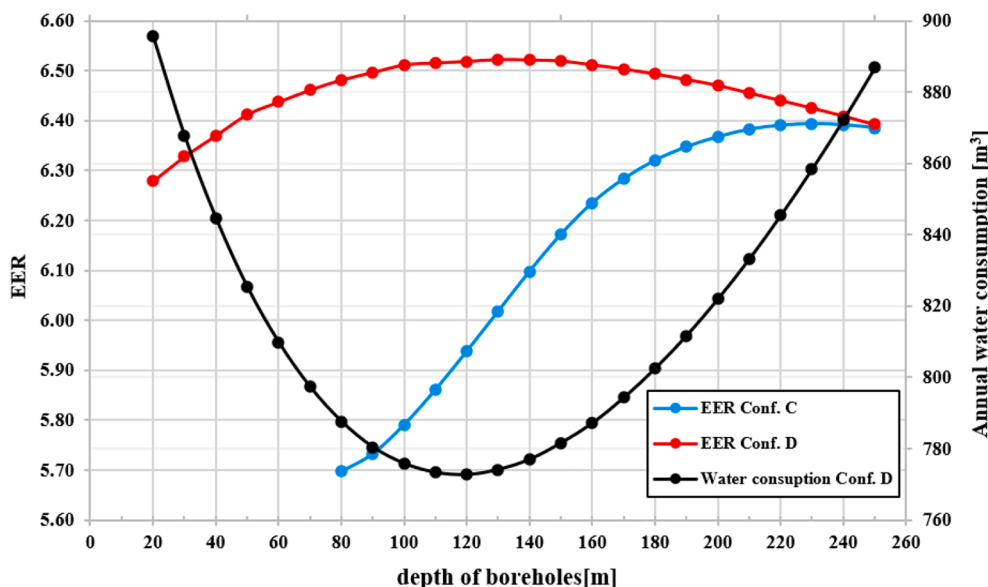
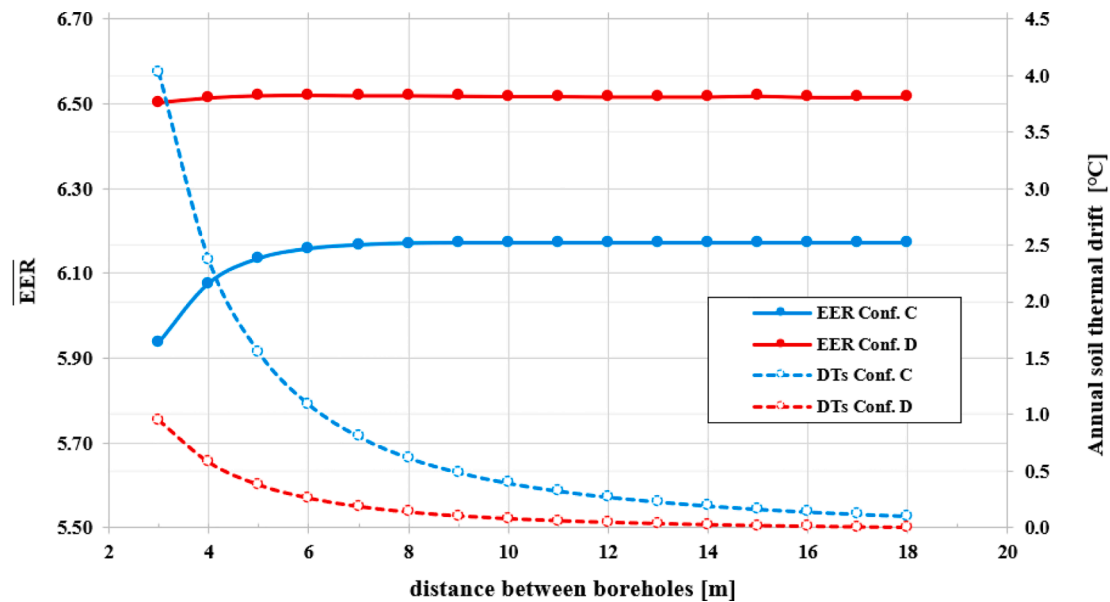**Fig. 12.** Sensitivity of system performance with BHE depth.

Fig. 13. Sensitivity of system performance with BHE distance.

performance is reduced when comparing simple and hybrid configurations with conventional water-cooled chillers equipped with CTs (less than 10%). However, substantial reductions in water consumption could be achieved. More specifically, compared to the conventional water-cooled chillers, no more water is consumed when a simple ground source multiple chillers system is considered. A 19.5% reduction in water consumption is observed with hybrid ground source multiple chillers systems.

The performed sensitivity analyses showed the capability of the developed model to support the design of these systems. For instance, varying the BHE depth, an optimal value of EER could be found in both configurations. Also, if the distance of the probes is greater than 10 m, an efficient operation of the plants is assured over the years due to the limited soil thermal drift. Meanwhile, the comparison of hourly temperature profiles of two typical working days showed the capability of the model to support the operation of these systems, providing insights on those variables which could limit the energy performance of the plant (either the air-wet bulb temperature or the average temperature of the soil).

Although this technology is usually preferred in a climate where heating demand is predominant, the results suggested that it could bring advantages also in a climate where cooling demand is not negligible. Indeed, the achieved energy saving will lead to a reduction of carbon dioxide emissions resulting from lower electricity consumed from the grid. Moreover, less water is withdrawn from nature. Future works will investigate the operation of such technology when both thermal and cooling demand are covered, including economic and environmental analyses as well.

CRediT authorship contribution statement

Alessandro Buscemi: Conceptualization, Software, Investigation, Methodology, Writing – original draft, Visualization. **Pietro Catrini:** Conceptualization, Software, Investigation, Methodology, Writing – original draft, Visualization. **Antonio Piacentino:** Conceptualization, Investigation, Methodology, Writing – review & editing, Visualization. **Fabio Cardona:** Data curation, Investigation. **Dhirendran Munith Kumar:** Data curation, Investigation.

Declaration of Competing Interest

The authors declare that they have no known competing financial interests or personal relationships that could have appeared to influence the work reported in this paper.

References

[1] International Energy Agency (IEA). https://www.iea.org/data-and-statistics 2019.
[2] Ürge-Vorsatz D, Cabeza LF, Serrano S, Barreneche C, Petrichenko K. Heating and cooling energy trends and drivers in buildings. Renew Sustain Energy Rev 2015;41: 85–98. https://doi.org/10.1016/j.rser.2014.08.039.
[3] Economidou M, Todeschi V, Bertoldi P, D'Agostino D, Zangheri P, Castellazzi L. Review of 50 years of EU energy efficiency policies for buildings. Energy Build 2020;225:110322. https://doi.org/10.1016/j.enbuild.2020.110322.
[4] Soltani M, M. Kashkooli F, Dehghani-Sanij AR, Kazemi AR, Bordbar N, Farshchi MJ, et al. A comprehensive study of geothermal heating and cooling systems. Sustainable Cities Society 2019;44:793–818.
[5] Lund JW, Toth AN. Direct Utilization of Geothermal Energy 2020 Worldwide Review. Proc World Geothermal Cong 2021;90:101915.
[6] Karytsas S, Choropanitis I. Barriers against and actions towards renewable energy technologies diffusion: A Principal Component Analysis for residential ground source heat pump (GSHP) systems. Renew Sustain Energy Rev 2017;78:252–71. https://doi.org/10.1016/j.rser.2017.04.060.
[7] Aditya GR, Mikhaylova O, Narsilio GA, Johnston IW. Comparative costs of ground source heat pump systems against other forms of heating and cooling for different climatic conditions. Sustainable Energy Technol Assess 2020;42:100824. https://doi.org/10.1016/j.seta.2020.100824.
[8] Atam E, Helsen L. Ground-coupled heat pumps: Part 1 – Literature review and research challenges in modeling and optimal control. Renew Sustain Energy Rev 2016;54:1653–67. https://doi.org/10.1016/j.rser.2015.10.007.
[9] Noorollahi Y, Saeidi R, Mohammadi M, Amiri A, Hosseinzadeh M. The effects of ground heat exchanger parameters changes on geothermal heat pump performance – A review. Appl Therm Eng 2018;129:1645–58. https://doi.org/10.1016/j.applthermaleng.2017.10.111.
[10] Zhai XQ, Qu M, Yu X, Yang Y, Wang RZ. A review for the applications and integrated approaches of ground-coupled heat pump systems. Renew Sustain Energy Rev 2011;15:3133–40. https://doi.org/10.1016/j.rser.2011.04.024.
[11] Kavian S, Aghanajafi C, Jafari Mosleh H, Nazari A, Nazari A. Exergy, economic and environmental evaluation of an optimized hybrid photovoltaic-geothermal heat pump system. Appl Energy 2020;276:115469. https://doi.org/10.1016/j.apenergy.2020.115469.
[12] Litjens GBMA, Worrell E, van Sark WGJHM. Lowering greenhouse gas emissions in the built environment by combining ground source heat pumps, photovoltaics and battery storage. Energy Build 2018;180:51–71. https://doi.org/10.1016/j.enbuild.2018.09.026.
[13] Alavy M, Peiris M, Wang J, Rosen MA. Assessment of a novel phase change material-based thermal caisson for geothermal heating and cooling. Energy Convers Manage 2021;234:113928. https://doi.org/10.1016/j.enconman.2021.113928.

[14] Cunha RP, Bourne-Webb PJ. A critical review on the current knowledge of geothermal energy piles to sustainably climatize buildings. Renew Sustain Energy Rev 2022;158:112072. https://doi.org/10.1016/j.rser.2022.112072.

[15] Bi Y, Wang X, Liu Y, Zhang H, Chen L. Comprehensive exergy analysis of a ground-source heat pump system for both building heating and cooling modes. Appl Energy 2009;86:2560–5. https://doi.org/10.1016/j.apenergy.2009.04.005.

[16] Jeon J, Lee S, Hong D, Kim Y. Performance evaluation and modeling of a hybrid cooling system combining a screw water chiller with a ground source heat pump in a building. Energy 2010;35:2006–12. https://doi.org/10.1016/j.energy.2010.01.016.

[17] Pardo N, Montero Á, Martos J, Urchueguía JF. Optimization of hybrid – ground coupled and air source – heat pump systems in combination with thermal storage. Appl Therm Eng 2010;30:1073–7. https://doi.org/10.1016/j.applthermaleng.2010.01.015.

[18] Park H, Lee JS, Kim W, Kim Y. The cooling seasonal performance factor of a hybrid ground-source heat pump with parallel and serial configurations. Appl Energy 2013;102:877–84. https://doi.org/10.1016/j.apenergy.2012.09.035.

[19] Mohammadzadeh Bina S, Fujii H, Tsuya S, Kosukegawa H. Comparative study of hybrid ground source heat pump in cooling and heating dominant climates. Energy Convers Manage 2022;252:115122. https://doi.org/10.1016/j.enconman.2021.115122.

[20] Chiasson AD, Yavuzturk C, Talbert WJ. Design of School Building HVAC Retrofit with Hybrid Geothermal Heat-Pump System. J Archit Eng 2004;10(3):103–11. https://doi.org/10.1061/(ASCE)1076-0431(2004)10:3(103).

[21] You T, Wu W, Yang H, Liu J, Li X. Hybrid photovoltaic/thermal and ground source heat pump: Review and perspective. Renew Sustain Energy Rev 2021;151:111569. https://doi.org/10.1016/j.rser.2021.111569.

[22] Gang W, Wang J, Wang S. Performance analysis of hybrid ground source heat pump systems based on ANN predictive control. Appl Energy 2014;136:1138–44. https://doi.org/10.1016/j.apenergy.2014.04.005.

[23] Hu B, Li Y, Mu B, Wang S, Seem JE, Cao F. Extremum seeking control for efficient operation of hybrid ground source heat pump system. Renewable Energy 2016;86:332–46. https://doi.org/10.1016/j.renene.2015.07.092.

[24] De Ridder F, Diehl M, Mulder G, Desmedt J, Van Bael J. An optimal control algorithm for borehole thermal energy storage systems. Energy Build 2011;43:2918–25. https://doi.org/10.1016/j.enbuild.2011.07.015.

[25] Marrasso E, Roselli C, Sasso M, Tariello F. Global and local environmental and energy advantages of a geothermal heat pump interacting with a low temperature thermal micro grid. Energy Convers Manage 2018;172:540–53. https://doi.org/10.1016/j.enconman.2018.07.028.

[26] Calise F, Cappiello FL, Dentice d'Accadia M, Petrakopoulou F, Vicidomini M. A solar-driven 5th generation district heating and cooling network with ground-source heat pumps: a thermo-economic analysis. Sustainable Cities Society 2022;76:103438.

[27] Urchueguía JF, Zacarés M, Corberán JM, Montero Á, Martos J, Witte H. Comparison between the energy performance of a ground coupled water to water heat pump system and an air to water heat pump system for heating and cooling in typical conditions of the European Mediterranean coast. Energy Convers Manage 2008;49:2917–23. https://doi.org/10.1016/j.enconman.2008.03.001.

[28] Frau C, Maggio E, Poggi F, Melis E, Floris F, Orrù PF. Low-enthalpy geothermal systems for air conditioning: a case study in the Mediterranean climate. Energy Procedia 2018;148:527–34. https://doi.org/10.1016/j.egypro.2018.08.129.

[29] Blázquez CS, Verda V, Nieto IM, Martín AF, González-Aguilera D. Analysis and optimization of the design parameters of a district groundwater heat pump system in Turin. Italy Renewable Energy 2020;149:374–83. https://doi.org/10.1016/j.renene.2019.12.074.

[30] Guarino S, Buscemi A, Ciulla G, Bonomolo M, Lo Brano V. A dish-stirling solar concentrator coupled to a seasonal thermal energy storage system in the southern mediterranean basin: A cogenerative layout hypothesis. Energy Convers Manage 2020;222:113228.

[31] Naldi C, Zanchini E. Effects of the total borehole length and of the heat pump inverter on the performance of a ground-coupled heat pump system. Appl Therm Eng 2018;128:306–19. https://doi.org/10.1016/j.applthermaleng.2017.09.025.

[32] Lazzarin R, Noro M. Photovoltaic/Thermal (PV/T)/ground dual source heat pump: Optimum energy and economic sizing based on performance analysis. Energy Build 2020;211:109800. https://doi.org/10.1016/j.enbuild.2020.109800.

[33] Iorio M, Carotenuto A, Corniello A, Di Fraia S, Massarotti N, Mauro A, et al. Low Enthalpy Geothermal Systems in Structural Controlled Areas: A Sustainability Analysis of Geothermal Resource for Heating Plant (The Mondragone Case in Southern Appennines, Italy). Energies 2020;13(5):1237.

[34] Sakellariou EI, Axaopoulos PJ, Wright AJ. Energy and economic evaluation of a solar assisted ground source heat pump system for a north Mediterranean city. Energy Build 2021;231:110640. https://doi.org/10.1016/j.enbuild.2020.110640.

[35] Baglivo C, Bonuso S, Congedo P. Performance Analysis of Air Cooled Heat Pump Coupled with Horizontal Air Ground Heat Exchanger in the Mediterranean Climate. Energies 2018;11(10):2704.

[36] Michopoulos A, Voulgari V, Tsikaloudaki A, Zachariadis Th. Evaluation of ground source heat pump systems for residential buildings in warm Mediterranean regions:

the example of Cyprus. Energ Effi 2016;9:1421–36. https://doi.org/10.1007/s12053-016-9431-1.

[37] Hellström G. Ground heat storage: Thermal analyses of duct storage systems. Lund University; 1991.

[38] Pahud D, Hellström G. The New Duct Ground Heat Model for TRNSYS. Eurotherm - Physical Models For Thermal Energy Stores 1996.

[39] Conti P, Testi D, Grassi W. Revised heat transfer modeling of double-U vertical ground-coupled heat exchangers. Appl Therm Eng 2016;106:1257–67.

[40] Claesson J, Javed S. Explicitmultipole formulas for calculating thermal resistance of single u-tube ground heat exchangers. Energies 2018;11(1):214.

[41] Gnielinski V. On heat transfer in tubes. Int J Heat Mass Transf 2013;63:134–40.

[42] Bejan A. Advanced Engineering Thermodynamics. Wiley; 2016.

[43] Lamarche L, Kajl S, Beauchamp B. A review of methods to evaluate borehole thermal resistances in geothermal heat-pump systems. Geothermics 2010;39(2):187–200.

[44] Claesson J, Javed S. Explicit multipole formulas and thermal network models for calculating thermal resistances of double U-pipe borehole heat exchangers. Sci Technol Built Environ 2019;25(8):980–92.

[45] DeWitt DP, Bergam TL, Lavine AS, Incropera FP. Fundamentals of Heat And Mass Transfer. 6th ed. John Wiley & Sons Inc; 2006.

[46] Cedergren HR. Seepage, drainage, and flow nets. (2nd edn.) 1977. doi:10.1016/0148-9062(78)91413-4.

[47] Davies JH, Davies DR. Earth's surface heat flux. Solid. Earth 2010;1(1):5–24.

[48] Panno D, Buscemi A, Beccali M, Chiaruzzi C, Cipriani G, Ciulla G, et al. A solar assisted seasonal borehole thermal energy system for a non-residential building in the Mediterranean area. Sol Energy 2019;192:120–32.

[49] IMST-Group Instituto de Ingeniería Energética Universidad Politécnica de Valencia. IMST-Art 2017.

[50] Corberán J-M, Martínez-Galván I, Gonzálvez-Maciá J, Martínez-Ballester S. Influence of the source and sink temperatures on the optimal refrigerant charge of a water-to-water heat pump. IIR 1st Workshop on Refrigerant Charge Reduction, France. 2009.

[51] Braun JE, Klein SA, Mitchell JW. Effectiveness Models for Cooling Towers and Cooling Coils. ASHRAE Trans 1989.

[52] Verdunstungshuhlung MF. Zeitschrift des Vereines Deutscher Ingenieure (VDI). Vol 1925;70:123–8.

[53] Cooling Technology Institute. Standard for the Certification of Water Cooling Tower Thermal - STD 201RS. 2019. Available at: https://www.coolingtechnology.org/.

[54] Baltimore Aircoil Company. VTL-E Cooling Tower performance data at standard conditions 2021. Available at: https://www.baltimoreaircoil.eu/en/products/VTL-E-039G-137M.

[55] Piacentino A, Barbaro C. A comprehensive tool for efficient design and operation of polygeneration-based energy μgrids serving a cluster of buildings. Part II: Analysis of the applicative potential. Appl Energy 2013;111:1222–38. https://doi.org/10.1016/J.APENERGY.2012.11.079.

[56] Catrini P, Piacentino A, Cardona F, Ciulla G. Exergoeconomic analysis as support in decision-making for the design and operation of multiple chiller systems in air conditioning applications. Energy Convers Manage 2020;220:113051. https://doi.org/10.1016/j.enconman.2020.113051.

[57] Klein SA. TRNSYS 17: A Transient System Simulation Program. Madison, USA: Solar Energy Laboratory, University of Wisconsin; 2010.

[58] Meteonorm: Meteonorm, Global Meteorological Database. 2015:Handbook part II: theory, version 7.1.7.201517.

[59] Sakellariou EI, Wright AJ, Axaopoulos P, Oyinlola MA. PVT based solar assisted ground source heat pump system: Modelling approach and sensitivity analyses. Sol Energy 2019;193:37–50. https://doi.org/10.1016/j.solener.2019.09.044.

[60] Xu L, Guo F, Hoes P-J, Yang X, Hensen JLM. Investigating energy performance of large-scale seasonal storage in the district heating system of chifeng city: Measurements and model-based analysis of operation strategies. Energy Build 2021;247:111113. https://doi.org/10.1016/j.enbuild.2021.111113.

[61] De Rosa M, Ruiz-Calvo F, Corberán JM, Montagud C, Tagliafico LA. Borehole modelling: a comparison between a steady-state model and a novel dynamic model in a real ON/OFF GSHP operation. J Phys Conf Ser 2014;547:012008. https://doi.org/10.1088/1742-6596/547/1/012008.

[62] Pitarch-Mocholi M, Navarro-Peris EE, Gonzalvez-Macia J, Corberan JM. Comparative analysis of two subcritical heat pump boosters using subcooling in order to increase the efficiency of systems with a high water temperature glide. 12th IEA Heat Pump Conference, Rotterdam. 2017.

[63] Air-Conditioning Heating and Refrigeration Institute. 2017-Standard for Performance Rating of Unitary Air-conditioning & Air-source Heat Pump Equipment. Air Conditioning, Heating, and Refrigeration Institute; 2017.

[64] Catrini P, Panno D, Cardona F, Piacentino A. Characterization of cooling loads in the wine industry and novel seasonal indicator for reliable assessment of energy saving through retrofit of chillers. Appl Energy 2020;266:114856. https://doi.org/10.1016/j.apenergy.2020.114856.